

The shear power spectrum from the COMBO-17 survey

M.L. Brown^{1*}, A.N. Taylor^{1*}, D.J. Bacon^{1*}, M.E. Gray¹, S. Dye², K. Meisenheimer³, & C. Wolf⁴

¹*Institute for Astronomy, University of Edinburgh, Blackford Hill, Edinburgh EH9 3HJ*

²*Astrophysics Group, Blackett Laboratory, Imperial College, Prince Consort Road, London SW7 2BW*

³*Max-Planck-Institut für Astronomie, Königstuhl 17, D-69117, Heidelberg, Germany*

⁴*Department of Physics, University of Oxford, Keble Road, Oxford OX1 3RH*

Accepted 2002 November 29. Received 2002 November 12; in original form 2002 October 9

ABSTRACT

We perform a statistical weak lensing or “cosmic shear” analysis of the COMBO-17 survey – a unique dataset with shear quality R-band imaging and accurate photometric redshift estimates ($\sigma_z = 0.05$) for $\sim 90\%$ of galaxies to $m_R \leq 24.0$. We undertake a full maximum likelihood analysis to measure directly from the data the weak lensing power spectra, $C_\ell^{\kappa\kappa}$, $C_\ell^{\beta\beta}$ and $C_\ell^{\kappa\beta}$ in 5 band powers from $\ell = 400$ to $\ell = 10^4$, where κ is the usual lens convergence and β is an odd-parity ‘curl’ component of the shear signal. We find a strong measurement of the convergence power over five fields. The non-gravitational β -field has a much lower significance, indicating our data is free of major systematics, while the cross-correlation of κ and β is consistent with zero. We have also calculated the shear correlation functions and variance over a range of scales between 0.5 and 20 arcmin. Our measurements of minimal star-galaxy correlations and cross-correlations between galaxy components provide further evidence that any systematics are negligible.

In addition, we have used our results to measure cosmological parameters, constraining the normalisation of the matter power spectrum to be $\sigma_8 = (0.72 \pm 0.09)(\Omega_m/0.3)^{-0.49}$, where the errors quoted are $1\text{-}\sigma$ due to the intrinsic dispersion in galaxy ellipticities, cosmic and sampling variance. We have significantly reduced the usual additional uncertainty in the median redshift (z_m) of the source galaxies by estimating z_m directly from our data using accurate photometric redshift information from the COMBO-17 multi-band wide-field survey. To demonstrate the power of accurate redshift information, we have also measured parameters from a shear analysis of only those galaxies for which accurate redshift estimates are available. In this case, we have eliminated the uncertainty in the redshift distribution of sources and we show that the uncertainty in the resulting parameter constraints are reduced by more than a factor of 2 compared to the typical uncertainties found in cosmic shear surveys to date. Finally, we combine our parameter measurements with constraints from the 2dF Galaxy Redshift Survey and with those from the CMB. With these additional constraints, we measure the normalisation of the matter power spectrum to be $\sigma_8 = 0.73^{+0.06}_{-0.03}$ and the matter density of the Universe to be $\Omega_m = 0.27^{+0.02}_{-0.01}$.

Key words: cosmology: observations - gravitational lensing, large-scale structure of the Universe

1 INTRODUCTION

There continues to be great interest and significant progress in measuring the weak lensing signal arising from large-scale structure. This phenomenon, observed as the weak coherent distortion

of background galaxies due to light ray deflection by intervening matter, offers us a direct probe of the mass distribution in the Universe. We can consequently measure cosmologically important quantities (see e.g.. Bernardeau et al. 1997; Jain & Seljak 1997; Kamionkowski et al. 1998; Kaiser 1998; Hu & Tegmark 1999) such as the bias (see e.g. Hoekstra et al. 2001) and the normalisation of the matter power spectrum (e.g. Bacon et al. 2002; Hoekstra et al. 2002; Refregier, Rhodes & Groth 2002; Van Waerbeke et al. 2002).

* mlb@roe.ac.uk; ant@roe.ac.uk; djb@roe.ac.uk

Of particular interest is the prospect of reconstructing the power spectrum of mass fluctuations from the weak lensing signal. Pen et al. (2002) have used an estimator for the weak lensing shear power spectrum, obtainable from correlation function measurements, to measure the shear power spectrum from the DESCART survey, while Schneider et al. (2002) have further developed estimators for this purpose. Meanwhile, Hu & White (2001) have demonstrated the utility of a maximum likelihood approach to reconstructing the shear power spectrum. Here we will apply a full maximum likelihood analysis to a cosmic shear survey for the first time.

In this paper, we describe the results of a weak shear analysis of the COMBO-17 dataset, acquired with the La Silla 2.2m telescope in Chile (Wolf et al. 2001). This survey includes 1.25 square degrees of deep R-band observations from which we draw our sample of background galaxies for shear measurements. In addition, the survey has yielded photometric redshifts for approximately 40% of the objects in our selected sample of galaxies, which we use to improve our understanding of the shear signal. We apply a maximum likelihood reconstruction to our dataset to obtain the shear power spectrum, and we fit cosmological models to measurements of both the shear power spectrum and the correlation functions to measure joint constraints on the matter density Ω_m and normalisation of the matter power spectrum σ_8 . We obtain further constraints on these parameters by combining our measurements with constraints from both the 2dF Galaxy Redshift Survey (2dFGRS, Percival et al. 2002) and from CMB data (e.g. Lewis & Bridle, 2002).

Cosmic shear studies require careful data reduction followed by assessment and removal of systematic effects, such as shear induced by a telescope, anisotropic point spread function (PSF), and circularization of galaxy shapes. We demonstrate in this paper that our shear catalogues have almost negligible systematic errors after applying appropriate corrections, and we carefully audit the remaining sources of error (from e.g. sample size, redshift uncertainty and shot noise) in order to interpret our results.

The paper is organized in the following fashion. In Section 2 we summarize the necessary formalism for our weak lensing analysis, including definitions of shear and the shear power spectrum. In Section 3 we describe the COMBO-17 survey. We then discuss the procedures used for data reduction, and describe our method for obtaining a shear catalogue fully corrected for systematic effects. Section 4 examines the individual COMBO-17 fields in detail, and explains our approach to including redshift information for these fields. We measure shear correlation functions and cell variance in Section 5, checking for residual systematics and comparing with the findings of other groups. Section 6 contains our likelihood analysis, resulting in shear power spectra measured for single fields and for the survey as a whole. In Section 7 we use our correlation functions and power spectra measurements to estimate cosmological parameters, taking into account the errors from sample size and redshift uncertainties. We then combine our constraints on these parameters with constraints obtained from the 2dFGRS and the CMB. In Section 8 we discuss these results and summarize our conclusions.

2 WEAK LENSING QUANTITIES

In the last few years weak gravitational lensing has emerged as the most direct method for measuring the distribution of matter, regardless of its nature, in the Local Universe (Mellier 1999, Bartelmann & Schneider 2001). This is largely due to its basis in well under-

stood physics: weak lensing is essentially a scattering experiment of photons off the gravitational field generated by cosmological structure. Here, we describe the various weak lensing fields and their statistical properties.

2.1 Weak lensing fields

Weak gravitational lensing induces a distortion into the images of distant source galaxies. This distortion can be parameterised by measuring the ellipticities,

$$e_{ij} = \begin{pmatrix} e_1 & e_2 \\ e_2 & -e_1 \end{pmatrix} \quad (1)$$

of each galaxy from its quadrupole moments at a given isophotal threshold (Kaiser, Squires and Broadhurst, 1995) or by examining the distortion to a set of orthogonal modes describing the galaxy shape (Refregier & Bacon 2003; Bernstein & Jarvis, 2002). In the first instance – which is the approach we adopt in the following analysis – the effect of lensing is to induce an additional ellipticity on the galaxy image;

$$e'_{ij} = e_{ij} + 2\gamma_{ij}, \quad (2)$$

where

$$\gamma_{ij} = \begin{pmatrix} \gamma_1 & \gamma_2 \\ \gamma_2 & -\gamma_1 \end{pmatrix} \quad (3)$$

is the trace-free lensing shear matrix. The components γ_1 and γ_2 of the shear matrix represent the two orthogonal modes of the distortion. The shear matrix is recoverable since in the absence of intrinsic alignments of galaxies, the galaxy ellipticities average to zero, $\langle e \rangle = 0$.

Since gravity is a potential theory in the weak-field regime, the shear field can be related to a lensing potential

$$\gamma_{ij} = \left(\partial_i \partial_j - \frac{1}{2} \delta_{ij}^K \partial^2 \right) \phi, \quad (4)$$

where $\partial_i \equiv r(\delta_{ij} - \hat{r}_i \hat{r}_j) \nabla_i$ is a dimensionless, transverse differential operator, and $\partial^2 \equiv \partial_i \partial^i$ is the transverse Laplacian. The indices (i, j) each take the values $(1, 2)$, and we have assumed a flat sky. On the scales currently of interest (i.e. from $\sim 100 h^{-1} \text{kpc}$ to $100 h^{-1} \text{Mpc}$), this is an excellent approximation.

The lensing potential is also observable via the lens convergence field

$$\kappa = \frac{1}{2} \partial^2 \phi, \quad (5)$$

which can be estimated from the weak magnification of sources,

$$\mu = |(1 - \kappa)^2 - \gamma^2|^{-1} \approx 1 + 2\kappa. \quad (6)$$

This can be measured from either the change in galaxy number density (Broadhurst, Taylor & Peacock 1995; Taylor et al. 1998) or from the change in size of sources (Bartelmann & Narayan, 1995). Although this has a lower signal-to-noise than the shear distribution, it is an independent estimator of the lensing potential.

The convergence field is related to the shear field by the differential relation, first used by Kaiser & Squires (1993);

$$\kappa = \partial^{-2} \partial_i \partial_j \gamma_{ij}, \quad (7)$$

where ∂^{-2} is the inverse 2-D Laplacian operator defined by

$$\partial^{-2} \equiv \frac{1}{2\pi} \int d^2 \hat{r}' \ln |\hat{r} - \hat{r}'|. \quad (8)$$

A useful quantity for tracing noise and systematics in gravitational lensing is the divergence-free field, β , defined by

$$\beta = \partial^{-2} \varepsilon_i^n \partial_j \partial_n \gamma_{ij}. \quad (9)$$

where ε_i^n is the Levi-Civita symbol in two dimensions,

$$\varepsilon_i^n = \begin{pmatrix} 0 & -1 \\ 1 & 0 \end{pmatrix}. \quad (10)$$

If γ_{ij} is generated purely by the lensing potential, this quantity vanishes. But if there are non-gravitational sources, due to noise, systematics or intrinsic alignments, β will be non-zero. In addition β terms can arise from finite fields, due to mode-mixing of the κ and β fields (Bunn, 2002).

In a spatially flat Universe, with comoving distance r we can relate the lensing potential and the gravitational potential by (e.g. Kaiser 1998; Hu 2000)

$$\phi(\mathbf{r}) = 2 \int_0^r dr' \left(\frac{r-r'}{rr'} \right) \Phi(\mathbf{r}'). \quad (11)$$

This equation assumes the Born approximation, in which the path of integration is unperturbed by the lens.

Although the lensing potential depends on the distance to the source galaxy, this dependence is usually lost by averaging all lensing quantities over the source distribution. However with redshift information the full 3-D character of lensing can be usefully recovered (Taylor 2001, Bacon & Taylor 2002, Hu & Keeton 2002).

Finally the Newtonian potential, Φ , can be related to perturbations in the matter density field, $\delta = \delta\rho_m/\rho_m$, by Poisson's equation;

$$\nabla^2 \Phi = 4\pi G \rho_m \delta a^2 = \frac{3}{2} \frac{\Omega_m}{a \lambda_H^2} \delta, \quad (12)$$

where we have introduced the cosmological scale factor a , the Hubble length $\lambda_H = c/H_0 \approx 3000 h^{-1} \text{Mpc}$, and the present-day mass-density parameter Ω_m . Here, H_0 is the Hubble constant and c is the speed of light.

2.2 Statistical properties

2.2.1 Shear covariance matrix

We may define a shear covariance matrix by

$$C_{ab}(\hat{\mathbf{r}}) = \langle \gamma_a(0) \gamma_b(\hat{\mathbf{r}}) \rangle, \quad (13)$$

where the indices (a, b) each take the values $(1, 2)$. Fourier transforming the shear field,

$$\gamma_{ij}(\boldsymbol{\ell}) = \int d^2 \hat{\mathbf{r}} \gamma_{ij}(\hat{\mathbf{r}}) e^{-i\boldsymbol{\ell} \cdot \hat{\mathbf{r}}}, \quad (14)$$

and decomposing it using equations (7) and (9), we may generate the shear power spectra from correlations of κ and β :

$$\begin{aligned} \langle \kappa(\boldsymbol{\ell}) \kappa^*(\boldsymbol{\ell}') \rangle &= (2\pi)^2 C_\ell^{\kappa\kappa} \delta_D(\boldsymbol{\ell} - \boldsymbol{\ell}'), \\ \langle \beta(\boldsymbol{\ell}) \beta^*(\boldsymbol{\ell}') \rangle &= (2\pi)^2 C_\ell^{\beta\beta} \delta_D(\boldsymbol{\ell} - \boldsymbol{\ell}'), \\ \langle \kappa(\boldsymbol{\ell}) \beta^*(\boldsymbol{\ell}') \rangle &= (2\pi)^2 C_\ell^{\kappa\beta} \delta_D(\boldsymbol{\ell} - \boldsymbol{\ell}'). \end{aligned} \quad (15)$$

The parity invariance of weak lensing suggests that $C_\ell^{\beta\beta} = C_\ell^{\kappa\beta} = 0$. However other effects, such as noise and systematics, as well as intrinsic galaxy alignments may give rise to a non-zero $C_\ell^{\beta\beta}$. Hence in our analysis we shall leave its amplitude to be determined by the data. The cross-correlation of $\kappa(\boldsymbol{\ell})$ and $\beta(\boldsymbol{\ell})$ is expected to be zero but it will also allow a second check on noise and systematics

in the shear field, and we shall treat it as another free function. In particular finite field and boundary effects can lead to leakage of power between these three spectra, which we shall attempt to monitor.

The shear power spectrum and the convergence power are related by

$$C_\ell^{\gamma\gamma} = C_\ell^{\kappa\kappa} \quad (16)$$

in the flat-sky approximation. For a spatially flat Universe, these are in turn related to the matter power spectrum, $P_\delta(k, r)$ by the integral relation (see e.g. Bartelmann & Schneider 2001):

$$C_\ell^{\kappa\kappa} = \frac{9}{4} \left(\frac{H_0}{c} \right)^4 \Omega_m^2 \int_0^{r_H} dr P_\delta \left(\frac{\ell}{r}, r \right) \left(\frac{\overline{W}(r)}{a(r)} \right)^2, \quad (17)$$

where a is the expansion factor and r is comoving distance. r_H is the comoving distance to the horizon:

$$r_H = c \int \frac{dz}{H(z)}, \quad (18)$$

where the Hubble parameter is given in terms of the matter density, Ω_m , the vacuum energy density, Ω_V and the spatial curvature, Ω_K as

$$H(z) = H_0 [(1+z)^3 \Omega_m + (1+z)^2 \Omega_K + \Omega_V]^{1/2}. \quad (19)$$

The weighting, \overline{W} , is given in terms of the normalised source distribution, $G(r) dr = p(z) dz$:

$$\overline{W}(r) \equiv \int_r^{r_H} dr' G(r') \frac{r' - r}{r'}. \quad (20)$$

The covariance of the components of the shear field are related to the power spectra by (Hu & White 2001)

$$\begin{aligned} C_{11}(\hat{\mathbf{r}}) &= \int \frac{d^2 \ell}{(2\pi)^2} \left(C_\ell^{\kappa\kappa} \cos^2 2\varphi_\ell + C_\ell^{\beta\beta} \sin^2 2\varphi_\ell \right. \\ &\quad \left. - C_\ell^{\kappa\beta} \sin 4\varphi_\ell \right) |W(\ell)|^2 e^{i\boldsymbol{\ell} \cdot \hat{\mathbf{r}}}, \\ C_{22}(\hat{\mathbf{r}}) &= \int \frac{d^2 \ell}{(2\pi)^2} \left(C_\ell^{\kappa\kappa} \sin^2 2\varphi_\ell + C_\ell^{\beta\beta} \cos^2 2\varphi_\ell \right. \\ &\quad \left. + C_\ell^{\kappa\beta} \sin 4\varphi_\ell \right) |W(\ell)|^2 e^{i\boldsymbol{\ell} \cdot \hat{\mathbf{r}}}, \\ C_{12}(\hat{\mathbf{r}}) &= \int \frac{d^2 \ell}{(2\pi)^2} \left(\frac{1}{2} (C_\ell^{\kappa\kappa} - C_\ell^{\beta\beta}) \sin 4\varphi_\ell \right. \\ &\quad \left. + C_\ell^{\kappa\beta} \cos 4\varphi_\ell \right) |W(\ell)|^2 e^{i\boldsymbol{\ell} \cdot \hat{\mathbf{r}}}, \end{aligned} \quad (21)$$

where $\cos \varphi_\ell = \hat{\boldsymbol{\ell}} \cdot \hat{\boldsymbol{\ell}}_x$ and $\hat{\boldsymbol{\ell}}_x$ is a fiducial wavenumber projected along the x-axis. We have included here a smoothing or pixelisation window function;

$$W(\boldsymbol{\ell}) = j_0(\ell_x \theta_{\text{pix}}/2) j_0(\ell_y \theta_{\text{pix}}/2), \quad (22)$$

where $j_0 = \sin(x)/x$ is the zeroth order spherical Bessel function and θ_{pix} is the smoothing/pixel scale.

2.2.2 The rotated shear correlation function

Another important two-point statistical measure of the weak lensing signal are the correlation functions, defined by

$$\begin{aligned} C_1(\boldsymbol{\theta}) &= \langle \gamma_1^r(\hat{\mathbf{r}}) \gamma_1^r(\hat{\mathbf{r}} + \boldsymbol{\theta}) \rangle, \\ C_2(\boldsymbol{\theta}) &= \langle \gamma_2^r(\hat{\mathbf{r}}) \gamma_2^r(\hat{\mathbf{r}} + \boldsymbol{\theta}) \rangle, \\ C_3(\boldsymbol{\theta}) &= \langle \gamma_1^r(\hat{\mathbf{r}}) \gamma_2^r(\hat{\mathbf{r}} + \boldsymbol{\theta}) \rangle, \end{aligned} \quad (23)$$

where the angled brackets denote the average over all galaxy pairs separated by an angle θ . The superscript, r denotes rotated shear components which are equivalent to γ_1 and γ_2 in a rotated coordinate frame, defined by the line joining the centroids of the two galaxies in question. In terms of the elements of the shear matrix (equation (3)), these rotated shear components are

$$\begin{aligned}\gamma_1^r &= \gamma_1 \cos(2\phi) + \gamma_2 \sin(2\phi) \\ \gamma_2^r &= -\gamma_1 \sin(2\phi) + \gamma_2 \cos(2\phi),\end{aligned}\quad (24)$$

where ϕ is the angle between the original and rotated coordinate frames. Once again, the parity invariance of weak lensing predicts that the cross-correlation function $C_3(\theta)$ should be zero. A non-zero $C_3(\theta)$ is, therefore, an indication of residual systematic effects present in the data. The correlation functions, $C_1(\theta)$ & $C_2(\theta)$ are related to the underlying convergence power spectrum via

$$C_i(\theta) = \int_0^\infty \frac{d\ell \ell}{4\pi} C_\ell^{\kappa\kappa} [J_0(\ell\theta) + (-1)^{i+1} J_4(\ell\theta)], \quad (25)$$

where $J_n(x)$ are Bessel functions.

2.2.3 Shear variance in cells

Finally, we can define the variance, $\sigma_\gamma^2(\theta)$ of the shear field, measured in circular cells of radius θ . In terms of the convergence power spectrum, this variance is

$$\sigma_\gamma^2(\theta) = \frac{1}{2\pi} \int_0^\infty d\ell \ell C_\ell^{\kappa\kappa} \left(\frac{2J_1(\ell\theta)}{\ell\theta} \right)^2. \quad (26)$$

In the following analysis, we have chosen to measure the shear variance in square cells of side length, θ . However, the corresponding variance in circular apertures can be recovered, to a good approximation, by scaling our measurements by $1/\sqrt{\pi}$ (e.g. Bacon, Regier & Ellis 2000).

Having considered the shear field and its statistical properties we now turn to our data set. In Sections 3 & 4 we describe the COMBO-17 dataset and our method used in producing the high quality deep R-band images from which we measure the shear field. In Sections 5 & 6 we shall use this data to determine the statistical properties of the observed shear field.

3 OBSERVATIONS AND DATA REDUCTION

3.1 The COMBO-17 survey

The observations analysed in this paper have been undertaken as part of the COMBO-17 survey (Wolf et al. 2001). This survey is being carried out with the Wide-Field Imager (WFI) at the MPG/ESO 2.2m telescope on La Silla, Chile. The survey currently consists of five $0.5^\circ \times 0.5^\circ$ fields totaling 1.25 square degrees with observations taken in five broad-band filters (*UBVRI*) and 12 narrow-band filters ranging from 420 to 914 nm. The chosen filter set facilitates accurate photometric redshift estimation ($\sigma_z \approx 0.05$) reliable down to an R-band magnitude of 24. During the observing runs, to facilitate accurate weak lensing studies, the best seeing conditions were reserved for obtaining deep R-band images of the five fields. It is these R-band images, along with the photometric redshift tables, that we make use of in this analysis.

3.2 Initial data processing

The initial reduction of the data proceeded along the lines of that described in Gray et al. (2002, hereafter GTM+). The WFI instrument consists of a 4×2 array of 2048×4096 pixel CCDs. With a pixel scale of $0.238''$, the resulting total field of view (FOV) of the WFI is $0.56^\circ \times 0.55^\circ$. The standard COMBO-17 pre-processing pipeline (Wolf et al. in prep.) produces mosaics of eight $2K \times 4K$ chip images which have been debiased, corrected for non-linearity, normalized, flat-fielded and cleaned of cosmic rays. The resulting mosaics have been simply skewed as an approximate correction for rotational mis-alignments between the chips. We have removed this skewing of the mosaiced images in order to restore the original chip configurations on the detector. The individual chip images were then extracted from the mosaics so that astrometric calibrations could be applied to each of the chip images individually.

3.3 The precise astrometric solution

After extraction from the mosaics, catalogues of objects were created for each chip exposure using SExtractor (Bertin & Arnouts 1996). Using pointing information from the image headers, an approximate transformation was calculated to convert the SExtractor (x, y) pixel coordinates of the objects to celestial coordinates (α, δ) for each exposure. These objects were then matched with objects from the digitized SuperCOSMOS Sky Survey (SSS)[†] (Hambly et al. 2001) to within a tolerance of $5''$. The resulting coordinate pairs were then used to iteratively calculate a linear astrometric solution for each chip image with the optical axis being used as the tangent point for projection. Typically around 300 objects per chip image were used for the final astrometric fits which had rms residuals of $\sim 0.2''$ (c.f. the pixel scale of $0.238''/\text{pixel}$). Including higher order terms and/or a radial distortion term in the astrometric solution has been investigated by GTM+. Although, in some cases, the fit was improved when a radial distortion term was included, they found no improvement for the instrument as a whole. Details concerning the artificial shear introduced by such a radial distortion are discussed in GTM+ who deduced a radial distortion of $\delta r/r \sim 0.025\%$ and a resulting instrumental shear pattern with amplitude $\gamma < 0.0001$. This level of distortion is clearly negligible in comparison to a typical Λ CDM cosmic shear signal of $\gamma \sim 0.01$ and so we have used the simple linear solution to perform astrometry on all the chip images. Further tests of the artificial shear introduced by both the WFI instrument and the telescope optics are described in the next section. Having produced linear astrometric fits for all the chip images in each of the five fields, these fits were then used to register the images to the same coordinate system. The images were thus aligned and combined, using 3σ bad pixel rejection with weighting by exposure time and scaling by the median pixel value. All bad columns and pixels were removed during the co-addition procedure due to the large number of images combined. The five resulting $8K \times 8K$ images were trimmed to remove the under-sampled edges of the fields resulting in five 8192×8192 pixel ($32.5' \times 32.5'$) images.

[†] Full access to the SSS is available via the World Wide Web at URL <http://www-wfau.roe.ac.uk>

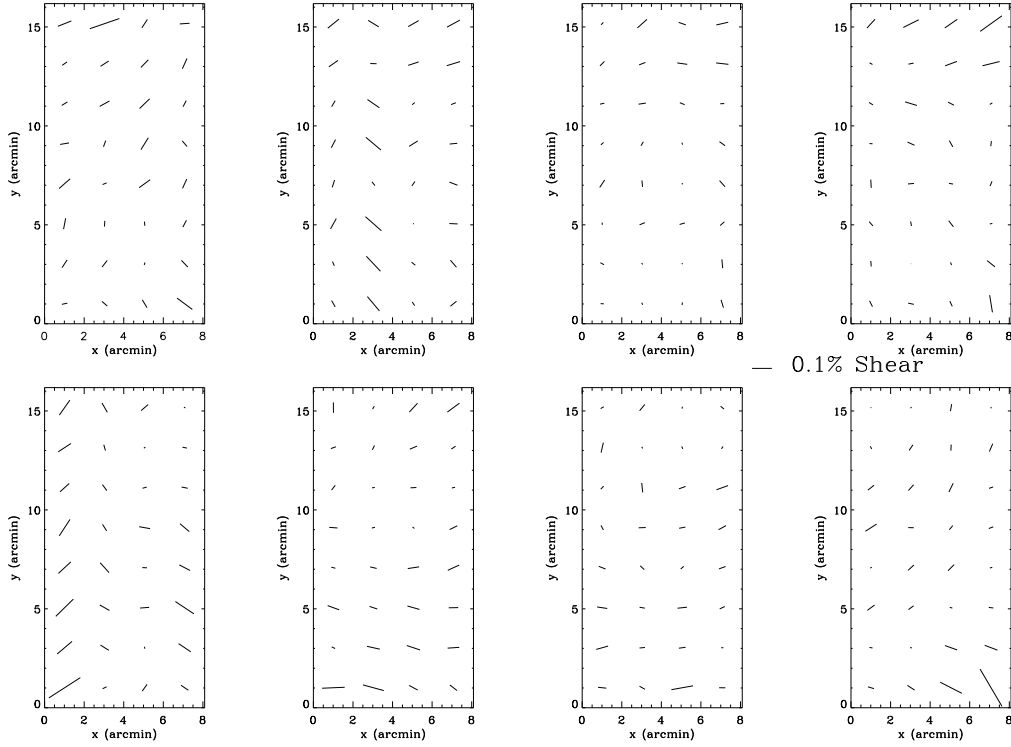


Figure 1. Instrumental shear pattern for the 8 chips of the WFI instrument as measured from the observed positions of the same objects on three dithered frames. The length of each vector represents the magnitude of the instrumental shear at the indicated position on the chip and the direction indicates the orientation of the distortion. For comparison, a 0.1% shear is also shown on the same scale.

3.4 Artificial shear introduced due to instrument and image co-addition

We have investigated the level of distortions introduced by the telescope optics and the WFI instrument by comparing the location of the same objects on dithered chip exposures. As documented in Bacon et al. (2000, hereafter BRE), the respective positions of the same object on two dithered frames, f and f' can be expressed as

$$\mathbf{x}^{f'} - \mathbf{x}^f \simeq \Psi(\bar{\mathbf{x}}^f - \bar{\mathbf{x}}^{f'}), \quad (27)$$

where \mathbf{x}^f ($\mathbf{x}^{f'}$) is the position of the object on frame f (f'), $\bar{\mathbf{x}}^f$ ($\bar{\mathbf{x}}^{f'}$) is the position of the centre of frame f (f') and Ψ is the distortion matrix, which may be expressed in terms of observables as

$$\Psi \equiv \begin{pmatrix} \kappa + \gamma_1 & \gamma_2 \\ \gamma_2 & \kappa - \gamma_1 \end{pmatrix}. \quad (28)$$

Here, κ and γ_i are the spurious convergence and shear introduced by the geometrical distortions. By measuring the positions of the same objects on three dithered frames, the resulting two equations of form (27) can be solved for κ and γ_i . We have used this method to map the instrumental distortion across the 8 component chips of the WFI and the resulting shear pattern is shown in Fig. 1 along with an indication of a 0.1% shear signal. We find, in agreement with GTM+, that the induced shear due to telescope and instrument distortions is indeed negligible ($\gamma < 0.2\%$) over the entire field compared to the typical weak lensing signal one would wish to measure.

We have also estimated the uncertainty introduced in the ellipticity measurements of objects on the combined images as a result of the co-adding procedure. Having registered the original exposures to the same coordinate frame, we then calculated the dispersion in the positions of many objects from the measured positions of those objects on all frames. We found a mean rms of ≈ 0.5 pixels in the positions of objects. Using this mean uncertainty in the position of objects, we can simulate the effect of image co-addition on a circular source of size ~ 0.7 arcsec, similar to the mean seeing disc size on the individual frames. We simulate the stacking of 78 frames (c.f. no. of frames for CDFS field - see Table 1) where we apply to each image an offset, $d\mathbf{x} = d\mathbf{x}^{\text{true}} + \delta\mathbf{x}$ where $d\mathbf{x}^{\text{true}}$ is the true offset position of the object and $\delta\mathbf{x}$ is a vector whose magnitude is taken from a Gaussian distribution centred on 0.5 pixels and whose orientation is taken from a uniform distribution between 0 and 2π . The size and ellipticity of the resulting stacked object was then computed using the formalism described in section 5.3 of BRE. Fig. 2 shows a histogram of the resulting ellipticity measurements for 1000 such simulations demonstrating that the shear arising from co-addition is again well below the sought-after cosmic shear signal. The median ellipticity induced in a circular source as measured from these simulations was $e_m = 0.0037$ and the inter-quartile range was $\delta e_m = 0.002$. These numbers are well within our error budget for a precise measurement of cosmic shear.

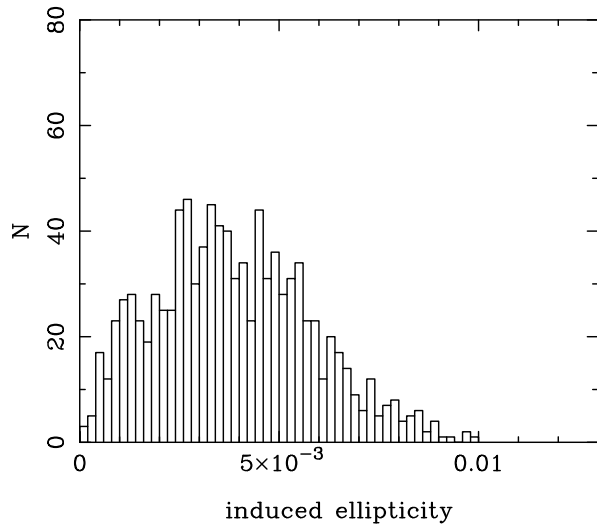


Figure 2. Ellipticity introduced in a circular source due to co-addition of individual frames as measured from 1000 simulations of the stacking of 78 frames.

3.5 Point spread function corrections and generation of object catalogues

We have used the *imcat* software (Kaiser, Squires and Broadhurst, 1995; hereafter KSB) to generate object catalogues for the five fields, measure shape parameters for all objects and to correct for such effects as the isotropic smearing of the point spread function (PSF) of objects by the atmosphere and telescope as well as any anisotropic smearing introduced by tracking errors, imperfect dither alignments and co-addition of the individual frames. We have used the *hfindpeaks* routine to locate objects, followed by the *getsky*, *apphot* and *getshapes* routines to estimate the local sky background, measure aperture magnitudes and half-light radii, r_h and to calculate shape parameters for all detected objects (see e.g. KSB; BRE; GTM+, for details of how the KSB procedure and the *imcat* software works).

This procedure produced an image catalogue for each field, containing positions, magnitudes, sizes and shapes for all the objects detected. We then applied reasonably conservative cuts on image size, signal-to-noise (S/N) and object ellipticity ($r_g > 1.0$, $\nu > 5$, $e < 0.5$) to remove spurious and/or untrustworthy detections. Note that the S/N cut we have used ($\nu > 5$) is much less stringent than that adopted in BRE who used a S/N cut of $\nu > 15$. The motivation in BRE for using such a conservative cut was the existence in their data of a highly significant anti-correlation between their measured mean shear values and the corresponding mean stellar ellipticities for a S/N cut of $\nu > 5$. We have searched for this effect in our data on several different smoothing scales and have found no evidence of correlations between our shear and stellar ellipticity values. For example, Fig. 3 shows the mean shear components in cells plotted against the mean uncorrected stellar ellipticity components for a cell size of 8×8 arcmin. This is the same cell size as that shown in BRE’s fig. 7 where a clear anti-correlation is present. It is clear from Fig. 3 however, that this effect is absent from our data. We have looked for such an effect on scales ranging from 1 to 30 arcmin and have found none. We have therefore used a $\nu > 5$ cut in our analysis. We also note that this is the same S/N cut as used in GTM+ for their supercluster analysis of the A901 field.

Having applied these cuts to the data, the *imcat* software was then used to correct the measured shapes of the galaxies for

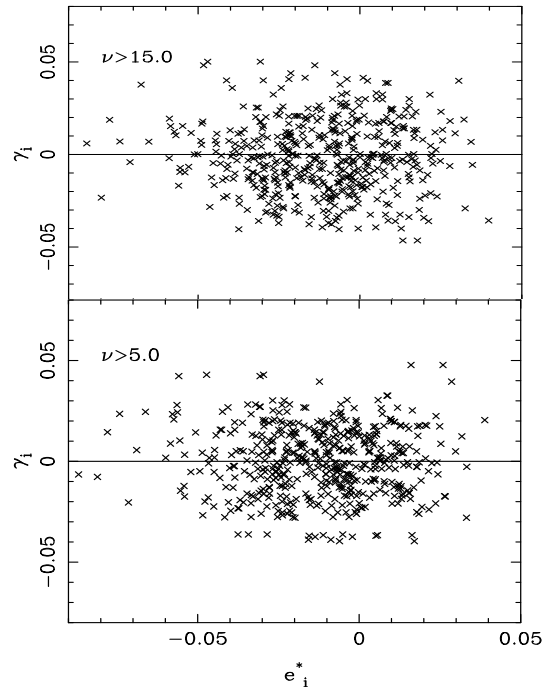


Figure 3. Mean shear components in cells plotted against the mean stellar ellipticity components for a cell size of 8×8 arcmin. The upper panel is for a S/N threshold of $\nu > 15$ and the lower panel is for a threshold of $\nu > 5$. The anti-correlation of γ_i with e_i^* found in the analysis of BRE is not present in the COMBO-17 data for either of the S/N cuts.

the effects mentioned above. In particular, we correct the galaxy shapes for (a) anisotropy and (b) circularization. Details of the correction scheme used by *imcat* have been described elsewhere (e.g. KSB; Luppino & Kaiser 1997; Hoekstra et al. 1998; Kaiser et al. 1999) and will not be repeated here. Note that these corrections were done on sections (size $8' \times 16'$) of the fields rather than the full $32.5' \times 32.5'$ fields themselves. This was done to ensure that an accurate model of the PSF distortions was obtained. Performing the corrections on the full fields would possibly lead to residual PSF distortions in the dataset due to inaccurate modelling of the stellar ellipticities over such a large field.

A demonstration of the anisotropic PSF correction at work for the S11 field is given in Figs. 4 and 5. The smoothly varying stellar ellipticity pattern apparent in the stars before correction (Fig. 5, left-hand side) is successfully removed to produce residual stellar ellipticities with essentially random orientations (Fig. 5, right-hand side) and mean residuals of $|\delta e_1| \approx 5 \times 10^{-4}$ and $|\delta e_2| \approx 2 \times 10^{-4}$. Fig. 4 shows the stellar ellipticities after correction randomly distributed about $e_1 = e_2 = 0$. Note however that these plots are for illustrative purposes only. Rigorous tests of the systematics introduced by residual spurious ellipticities are performed later in Section 5, where we measure the star-galaxy cross-correlation functions for the dataset.

4 THE COMBO-17 FIELDS

4.1 Content of the fields

The five fields observed are quite different from one another in terms of their content. Three are blank fields; one (CDF5) was chosen so it would overlap with the Chandra Deep Field South; another

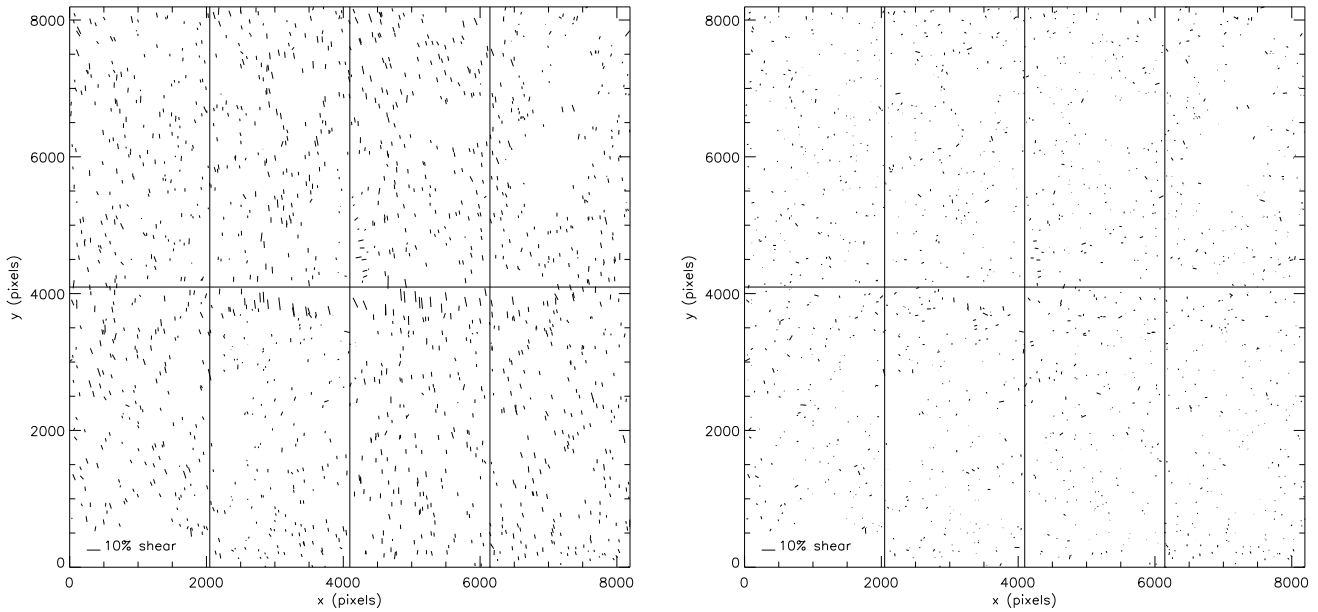


Figure 5. Stellar ellipticity pattern across the S11 field before (*left*) and after (*right*) correction for PSF anisotropy. A 10% shear signal is also shown for comparison. The horizontal and vertical lines show the sections used for the stellar ellipticity polynomial model fitting.

Table 1. Properties of the five COMBO-17 shear catalogues. In the sixth column we quote the median R-band magnitude of each catalogue. In the case of the SGP and FDF fields, the median m_R listed is an approximate value as magnitudes for these fields have been roughly calibrated using the APM galaxy survey. The mean galaxy density values (n_{gal}) are calculated as $n_{\text{gal}} = N_f/A_f$ where N_f and A_f are the total number of galaxies in the final shear catalogues and the total useable area of the fields respectively, after excluding regions contaminated by bright stars, diffraction spikes and ghosting (see Fig. 6). The FWHM values listed are the average FWHM of stars on each field as measured from the final co-added images. The final column indicates whether photometric redshift information is currently available for the field.

Field	RA(2000)	Dec.(2000)	R-band Exposures	Total Exp. Time	Median m_R	n_{gal} (arcmin $^{-2}$)	FWHM	Redshift info.?
CDFS	03 ^h 32 ^m 25 ^s	−27° 48′ 50″	42 × 500s + 36 × 420s	36120s	24.4	37.5	0.81″	Yes
SGP	00 ^h 45 ^m 56 ^s	−29° 35′ 15″	42 × 500s	21000s	23.6	36.2	0.81″	Pending
FDF	01 ^h 05 ^m 49 ^s	−25° 51′ 42″	20 × 500s + 5 × 400s	12000s	23.7	28.4	0.82″	No
S11	11 ^h 42 ^m 58 ^s	−01° 42′ 50″	39 × 400s + 5 × 500s	18100s	23.7	27.7	0.78″	Yes
A901	09 ^h 56 ^m 17 ^s	−10° 01′ 25″	36 × 500s + 8 × 600s	22800s	24.0	36.1	0.76″	Yes

(SGP) is centred on the South Galactic Pole, and the third blank field is the shallower FORS deep field (FDF). A fourth, randomly selected field (S11) contains a fairly large cluster (Abell 1364) at a redshift of $z = 0.11$. The fifth field (A901) was chosen so as to include a supercluster system (Abell 901/902) at redshift $z = 0.16$ and the COMBO-17 observations of this field have already been the subject of an extensive weak lensing analysis, details of which are given in GTM+. Details of the R-band observations for the five fields are given in Table 1. Note that we do not currently have the full 17-band photometric information for the SGP or FDF fields.

The significant mass concentrations present in the two fields containing clusters (S11 & A901) raise the question as to whether these fields should be included in a cosmic shear analysis at all. The significant difference between these fields is the pre-selection of A901 to include a supercluster system. Strictly speaking, therefore, the A901 field is not a randomly selected piece of sky and is unlikely to be a fair representation of the Universe. We have therefore chosen not to include this field in our final parameter estimation and shear power spectrum calculations. We have also experimented with including/excluding both the S11 and A901 fields from the

analysis. For both the shear power spectrum reconstruction and the parameter estimation, we find that the A901 field biases our results significantly, whereas the S11 field is consistent with the dataset as a whole (see Section 6.3). The cell-averaged shear distributions for the five fields are shown in Fig. 6, showing regions in the fields which have been masked out due to contamination by bright stars, diffractions spikes and ghosting.

4.2 Including redshift information

As mentioned earlier, the COMBO-17 survey has the unique advantage, in terms of weak lensing surveys, of having accurate photometric redshift measurements for $\sim 90\%$ of objects detected down to a magnitude of $m_R \leq 24$ (for a detailed description of the photometric methods used to assign redshifts to the galaxies, see Wolf et al. 2003). For these galaxies, the estimated typical uncertainty in redshift is $\sigma_z \sim 0.05$. At the time of writing, photometric data is available for three of our five fields (CDFS, A901 & S11). We have used this information to estimate, directly from the data, the redshift distribution and in particular, the median redshift, z_m of

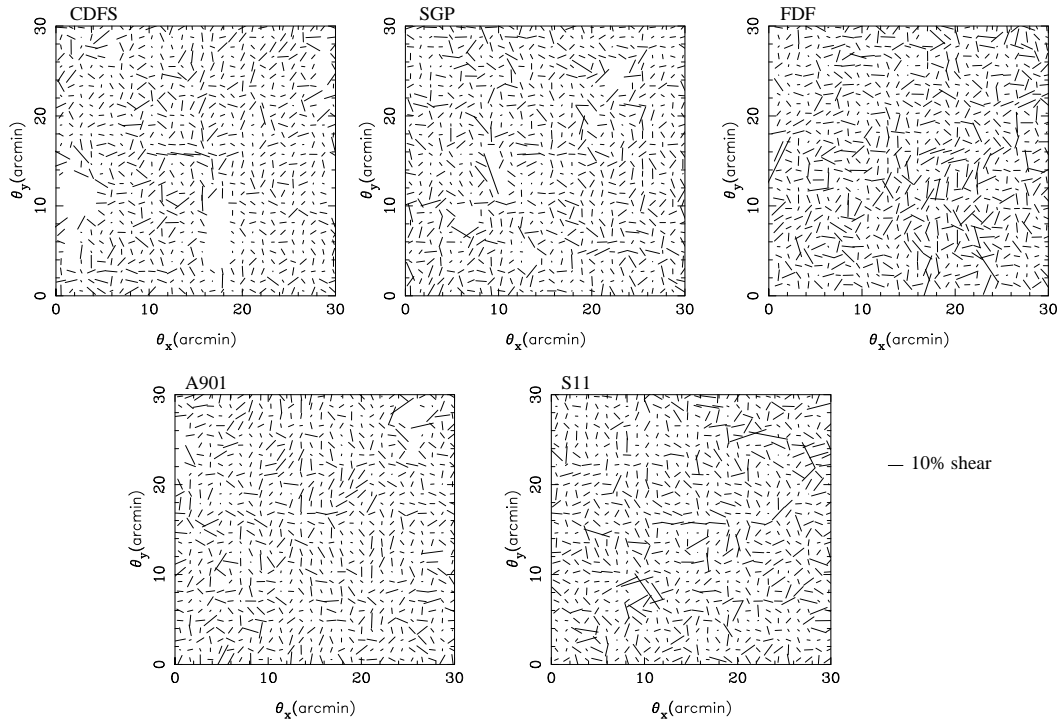


Figure 6. The shear distribution on the five COMBO fields. The fields are (clockwise from top left) CDFS, SGP, FDF, S11 and A901. The shear measurements for each field have been binned into 30×30 pixels, giving a pixel scale of ~ 1 arcmin. For each pixel, the length of the vector drawn is proportional to the magnitude of the mean shear in that pixel and its direction indicates the orientation of the shear. A 10% shear signal is also shown for comparison. The apparent holes in the distributions are regions which have been masked out due to bright stars, diffraction spikes etc.

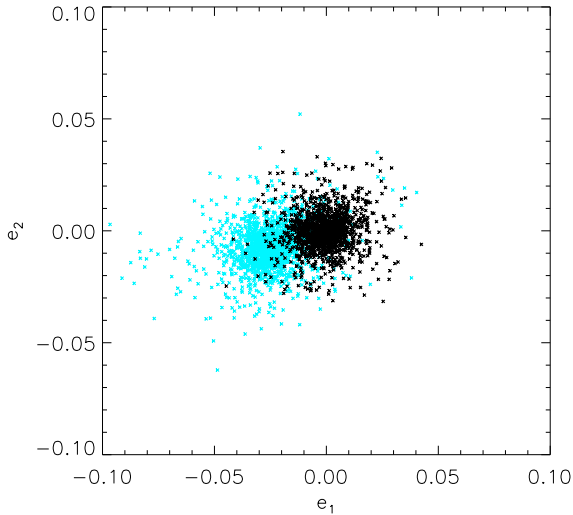


Figure 4. Ellipticity distribution of stars in the S11 field before (grey crosses) and after (black crosses) correction for PSF anisotropy. Mean stellar ellipticity components of $\bar{e}_1 = -0.025 \pm 0.013$ and $\bar{e}_2 = -0.007 \pm 0.011$ are removed to leave an essentially randomly orientated stellar ellipticity distribution with mean residual components of $\delta\bar{e}_1 = -0.0005 \pm 0.010$ and $\delta\bar{e}_2 = -0.0002 \pm 0.009$.

the lensed source galaxies in the survey. For the z_m calculation, we have only included those galaxies used in the final weak lensing analysis. This subset of galaxies does, in fact, include galaxies with magnitudes $m_R > 24$ for which the redshift estimations are unreliable. To account for this, we must extrapolate the redshift distribu-

Table 2. Measured median magnitudes and redshifts (z_m) for the three fields, CDFS, A901 & S11 for different limiting magnitude cut-offs. Also listed are the number of galaxies (N_{gal}) used in the median calculations and the completeness of each magnitude-limited sample (i.e. the fraction of galaxies in the sample for which accurate redshifts have been obtained). Extrapolating the median $m_R - z_m$ relation (see Fig. 7) to the median magnitude of the combined shear catalogues for all fields ($= 24.0$), we infer a median redshift for the COMBO-17 weak lensing survey of $z_m = 0.85 \pm 0.05$.

Limiting m_R	N_{gal}	Median m_R	z_m	Completeness
< 20.0	1485	19.15	0.184 ± 0.004	87%
< 21.0	3267	20.13	0.285 ± 0.030	87%
< 22.0	7316	21.14	0.404 ± 0.026	88%
< 23.0	16387	22.14	0.520 ± 0.023	87%
< 24.0	31649	22.96	0.673 ± 0.092	76%

tion beyond $m_R = 24$. For the three fields for which photometric data is available, accurate redshifts have been found for 31649 out of the 83514 galaxies used in the final shear analysis ($\sim 38\%$).

For a number of different limiting magnitudes, we have measured the median magnitude of the galaxies and the corresponding median redshift (z_m) of those same galaxies. Details of these measurements are given in Table 2. We take our median redshift measurements as lower limits for the true median redshift as the magnitude-limited samples are not complete in redshift (see Table

2) and those galaxies without an assigned redshift are most likely to be at a higher redshift than our measured median value. To calculate an upper limit for our z_m estimates, for each magnitude limited sample, we have placed those galaxies without redshift measurements at $z = \infty$ and have re-calculated z_m . We take our final median redshift estimate to be simply the midpoint between our upper and lower limits.

We have then extrapolated the median $m_R - z_m$ relation to find an estimate of the median redshift of our galaxy sample as a whole, which has a measured median magnitude of 24.0. The median $m_R - z_m$ relation is shown in Fig. 7. Here we plot both the COMBO-17 data points and data from the HDF redshift survey of Cohen et al. 2000, with which we are fully compatible. The curve plotted is the best-fit quadratic model to the COMBO-17 data and is given by

$$z_m = 2.53 - 0.33 m_{R,m} + 0.01 m_{R,m}^2. \quad (29)$$

where $m_{R,m}$ is the median R band magnitude of the galaxy sample. From this, we estimate a median redshift of $z_m = 0.85 \pm 0.05$ for the COMBO-17 weak lensing survey.

There is, of course, more information in the measured redshift distribution than just the median value. The advantage of including photometric information in a weak lensing analysis lies in reducing or eliminating uncertainties in the redshift distribution of the source galaxies when it comes to comparing weak lensing measurements with those predicted from theory (see Sections 6 & 7). To this end, we have included the measured redshift distribution for our comparison with theoretical models. There are, of course, many more galaxies for which we have no redshift estimate than there are galaxies with reliable measurements. This situation will improve as the COMBO-17 survey nears completion, but for the purposes of this analysis and predicting the expected weak lensing signal for different cosmological scenarios, we need to assign redshifts to the galaxies with unknown redshifts. We do this by distributing these galaxies in z according to (Baugh & Efstathiou 1991)

$$\frac{dN}{dz} = \frac{\beta z^2}{z_*^3} \exp \left[- \left(\frac{z}{z_*} \right)^\beta \right], \quad (30)$$

with $\beta = 1.5$ and $z_* = z_m/1.412$. A distribution of the form, equation (30) has a median redshift of z_m . We have tuned the value of z_m in equation (30) to ensure that the final *total* redshift distribution has a measured median value of $z_m = 0.85$.

After assigning values to the galaxies with unknown redshifts according to equation (30), we now have the final $n(z)$ distribution which we can use for making predictions for the weak lensing signal expected in the COMBO-17 survey. This final $n(z)$ distribution is shown in Fig. 8.

5 CORRELATION FUNCTIONS AND SHEAR VARIANCE ESTIMATORS

It is useful to estimate the correlation functions of the shear field both as a first approach at measuring the strength of the cosmic shear signal, but also as a test for unwanted systematics in the data. These tests have now become a standard part of shear analysis (e.g. Van Waerbeke et al. 2001; Pen, Van Waerbeke & Mellier 2002; Bacon et al. 2002). Measuring correlation functions also allows a direct comparison of our measurements with previous cosmic shear studies. Here we present both an unweighted correlation function analysis and a minimum variance weighted shear variance analysis. Note that, for the remainder of the paper, we have excluded

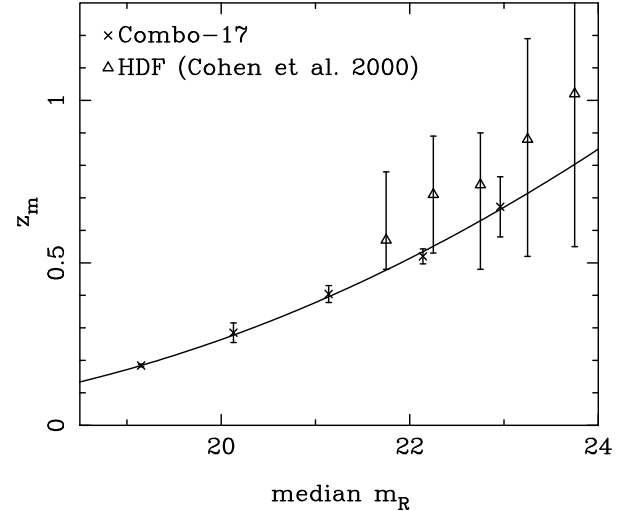


Figure 7. The dependence of the median redshift (z_m) of the COMBO-17 galaxies on the median magnitude of the galaxies as measured from the 3 fields for which we have photometric data. A simple quadratic model (solid curve) for the $m_R - z_m$ relation is also plotted for comparison. For our final weak lensing dataset, which has a median R -band magnitude of $m_R = 24.0$, we infer from this trend a median redshift of $z_m = 0.85 \pm 0.05$.

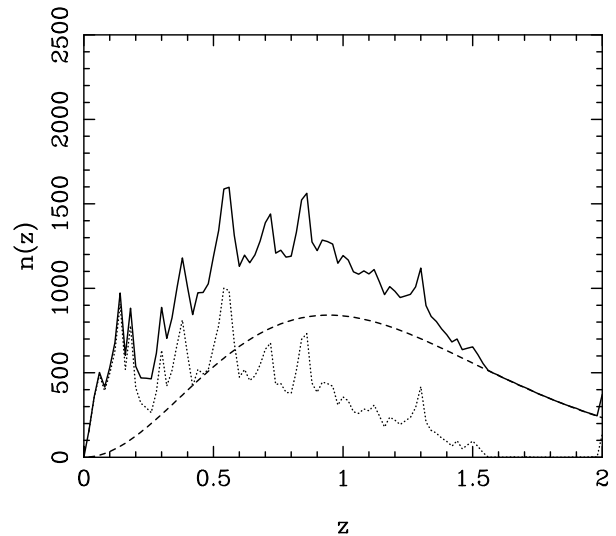


Figure 8. The final redshift distribution (solid line) used for making model predictions to compare with the observed weak lensing signal from the COMBO-17 dataset. This composite distribution has a median redshift of $z_m = 0.85$ and is composed of a measured $n(z)$ distribution (from the three fields, CDFS, S11 and A901; shown here as the dotted line) and a parameterised model (equation (30); dashed line) for the galaxies with unknown redshifts.

the A901/2 supercluster field from our measurements except where specifically indicated.

5.1 Correlation analysis

To estimate the unweighted correlation functions, we follow Bacon et al. (2002). For the purposes of the correlation analysis, we have divided each of the COMBO-17 fields into eight, chip-sized sections. This allows for a better estimate of the field-to-field covariance between our measurements than would be possible using the original $0.5^\circ \times 0.5^\circ$ fields. The correlation functions for the individual sections can be measured by averaging over galaxy pairs:

$$\begin{aligned} C_{1,s}(\theta) &= \frac{1}{n_s} \sum_{i=1}^{n_s} \gamma_1^r(\hat{r}_i) \gamma_1^r(\hat{r}_i + \theta), \\ C_{2,s}(\theta) &= \frac{1}{n_s} \sum_{i=1}^{n_s} \gamma_2^r(\hat{r}_i) \gamma_2^r(\hat{r}_i + \theta), \\ C_{3,s}(\theta) &= \frac{1}{n_s} \sum_{i=1}^{n_s} \gamma_1^r(\hat{r}_i) \gamma_2^r(\hat{r}_i + \theta), \end{aligned} \quad (31)$$

where n_s is the number of pairs of galaxies in each section and where we average over all galaxy pairs separated by an angle, θ (c.f. equation (23)). The signal averaged over all sections is simply

$$\bar{C}_i(\theta) = \frac{1}{N_s} \sum_{s=1}^{N_s} C_{i,s}(\theta), \quad (32)$$

where N_s is the total number of sections. The covariance of the correlation function measurements is given by

$$\begin{aligned} \text{cov}[\bar{C}_i(\theta) \bar{C}_j(\theta')] &\simeq \\ &\frac{1}{N_s^2} \sum_{s=1}^{N_s} [C_{i,s}(\theta) - \bar{C}_i(\theta)] [C_{j,s}(\theta') - \bar{C}_j(\theta')]. \end{aligned} \quad (33)$$

Fig. 9 shows the correlation functions, $C_1(\theta)$ and $C_2(\theta)$ after averaging over all sections of the four fields, CDFS, S11, SGP and FDF. As can be seen, our data agrees well with the expected correlations, for both C_1 and C_2 , for a $\Omega_m = 0.3$ Λ CDM model with a power spectrum normalisation of $\sigma_8 = 0.8$ (see Section 7 for our measurements of Ω_m & σ_8 from COMBO-17). These theoretical curves have been calculated using equation (25) where we have used the halofit model of Smith et al. (2002)[‡] to calculate the non-linear matter power spectrum. We have also input our combined redshift distribution (Fig. 8) into the calculation. We should point out that on smaller scales than those shown on Fig. 9, i.e. $\theta \lesssim 0.3$ arcmin, we have measured an inconsistently large signal ($\gtrsim 5 \times 10^{-4}$) for the C_1 correlation function. We suspect that this greatly enhanced signal is probably due to either systematic effects on very small scales due to imperfections in the correction for PSF anisotropy, or alternatively, the increased signal may be caused by intrinsic alignments dominating at such small angular separations. Either way, we exclude this single data point for our parameter estimations in Section 7. We also note that the errorbars on $C_1(\theta)$ and $C_2(\theta)$ may be slightly underestimated on the very largest scales due to correlations between neighbouring sections of the same field. Fig. 10 shows the cross-correlation between shear components, $C_3(\theta)$ which is consistent with zero, as expected.

In Fig. 11, we show the star-galaxy cross-correlations for our data. The systematically-induced cross-correlation between the

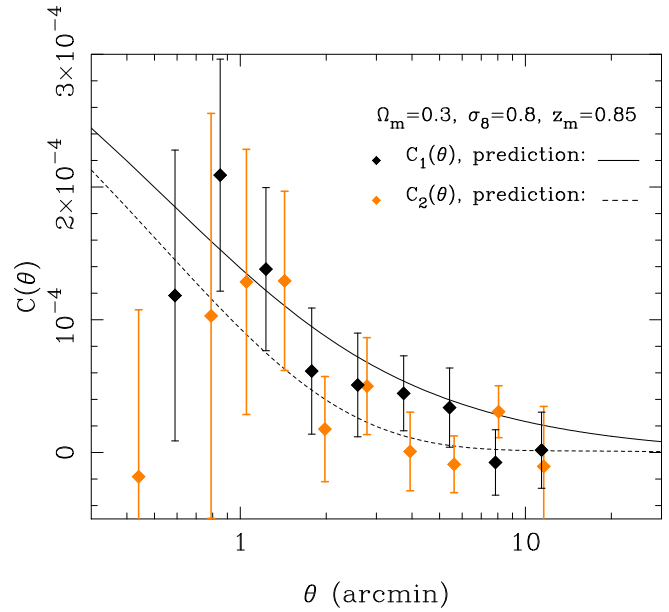


Figure 9. The unweighted shear correlation functions $C_1(\theta)$ and $C_2(\theta)$ from the COMBO-17 data. The solid dark line is the expected C_1 correlation for a $\Omega_m = 0.3$ Λ CDM model, normalised to $\sigma_8 = 0.8$, while the lighter dashed line is the expected C_2 signal. The C_2 points have been slightly displaced horizontally for clarity. Note that we measure an inconsistently large C_1 signal ($> 5 \times 10^{-4}$) on the very smallest scales ($\theta < 0.3$ arcmin, not shown) which, we suspect is due to residual systematic effects and/or intrinsic alignments.

galaxies (corrected for PSF anisotropy) and the uncorrected stars is defined by (Bacon et al. 2002):

$$C_i^{\text{sys}} = \frac{\langle \gamma_i e_i^* \rangle^2}{\langle e_i^* e_i^* \rangle}, \quad (34)$$

where $i = 1, 2$. A correlation here would indicate a problem in the correction of systematic image distortions. Again we find that no correlations are detected at scales $\theta \gtrsim 0.3$ arcmin, indicating that our PSF correction procedure has worked well. Note, however that the star-galaxy cross-correlations are significant at scales $\theta < 0.3$ arcmin, indicating a possible systematic problem at these very small scales – this motivates our exclusion of the smallest-scale $C_1(\theta)$ data point for our parameter estimations in Section 7.

We can use our correlation function measurements to compare our results with those of previous cosmic shear studies. We perform such a comparison by looking at the total correlation function, $C(\theta) = C_1(\theta) + C_2(\theta)$ for each data set. In Fig. 12, we plot $C(\theta)$ as measured from COMBO-17, along with the most recent results from four other groups (Van Waerbeke et al. 2001; Bacon et al. 2002; Refregier et al. 2002; Hoekstra et al. 2002). Note that we have scaled each groups' results to a median redshift of $z_s = 0.85$ using the scaling suggested by the numerical simulations of Barber (2002), i.e. $C(\theta) \propto z_m^2$. We have also, in the case of Refregier et al., and Hoekstra et al., assumed that $\sigma_\gamma^2(\theta) \approx C(\theta)$, where $\sigma_\gamma^2(\theta)$ is the shear variance statistic measured by these two groups. That this is a reasonable assumption can be seen by comparing the $\sigma_8 = 0.9$ models in Figs. 12 and 13. Fig. 12 shows that, beyond a scale of $\theta \sim 1$ arcmin, all groups are in broad agreement with each other, although the COMBO-17 signal does seem to be slightly lower in amplitude. At scales smaller than 1 arcmin, comparisons are more difficult to make because of the larger error bars

[‡] the halofit code is publicly available at URL <http://www.as1.chem.nottingham.ac.uk/~res/software.htm>

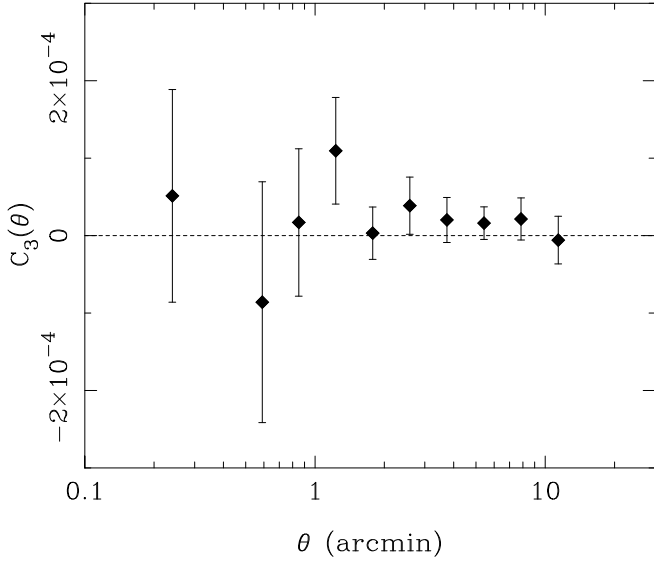


Figure 10. The cross-correlation of the shear components $C_3(\theta)$, as measured from the COMBO-17 dataset. The signal is consistent with zero on all scales in agreement with theoretical predictions.

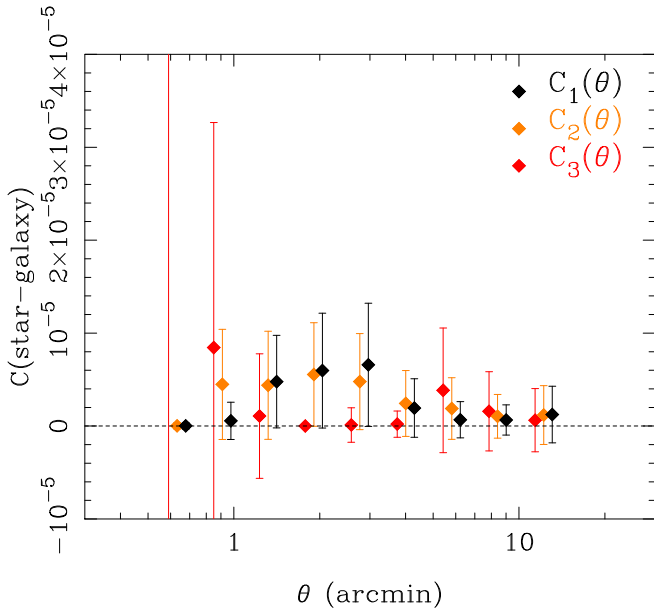


Figure 11. The star-galaxy cross-correlation functions (equation (34)) for the COMBO-17 data. The C_1 and C_2 points have been slightly offset horizontally for clarity. These measurements are a strong test of how successfully the galaxies have been corrected for distortions introduced by PSF anisotropy. The residual correlations between galaxies and stars are consistent with zero on all scales. In the worst-case scenario, represented by the upper end of the error bars shown, our correlation function measurements would include $< 10\%$ contamination from residual distortions left over from the PSF corrections applied.

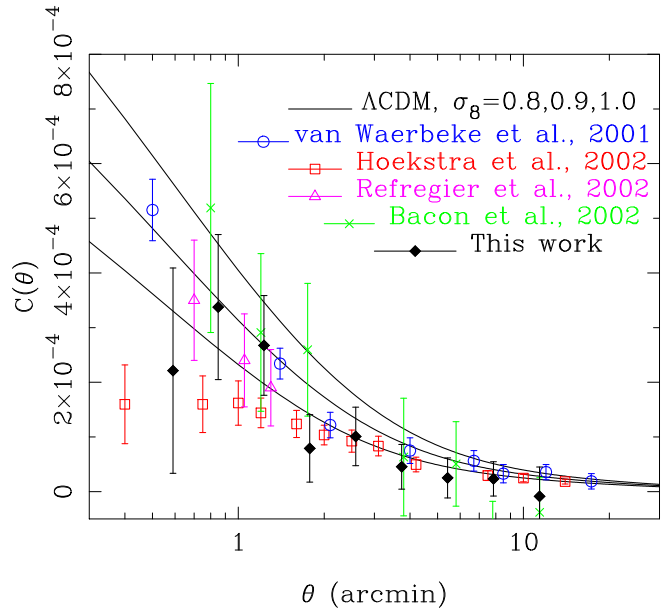


Figure 12. The total correlation function, $C(\theta)$, as measured from COMBO-17, along with the most recent cosmic shear measurements from the four other groups indicated. Beyond a scale of 1 arcmin, the measurements are in broad agreement. The correlation function predictions for a flat Λ CDM cosmology, for three values of the power spectrum normalisation (from top to bottom: $\sigma_8 = 1.0, 0.9, 0.8$) are also plotted.

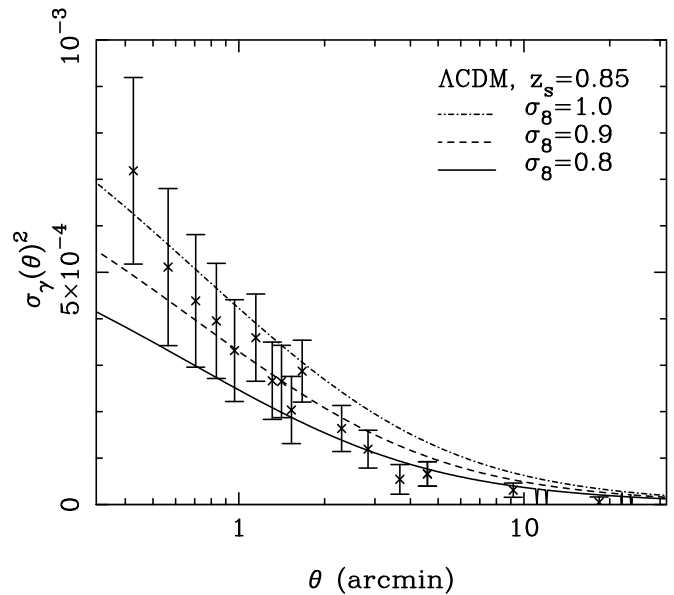


Figure 13. The minimum variance shear variance as measured from the COMBO-17 dataset. Also plotted are predictions for the shear variance for a $\Omega_m = 0.3$ Λ CDM cosmology for three different normalisations of the matter power spectrum.

involved. Indeed, it is the measurements at the larger scales ($\theta \gtrsim 1$ arcmin) that provide our best constraints on cosmological models.

5.2 Shear variance

We have also applied the minimum variance estimator of Brown et al. (2002) to measure the shear variance in square cells in excess of the noise:

$$\sigma_{\text{lens}}^2(\theta) = \frac{\sum_{\text{cell}} w_{\text{cell}} (e_{\text{cell}}^2 - N_{\text{cell}})}{\sum_{\text{cell}} w_{\text{cell}}}, \quad (35)$$

where e_{cell} is the cell averaged ellipticity and w_{cell} is a minimum variance weight;

$$w_{\text{cell}} = \frac{1}{2[\sigma_\gamma^4(\theta) + N_{\text{cell}}^2(\theta)]}. \quad (36)$$

Here N_{cell} is the noise in the cell measured from the data due to the intrinsic dispersion in galaxy ellipticities,

$$N_{\text{cell}}(\theta) = \frac{1}{n^2} \sum_{i=1}^n (e_1^2(\hat{\mathbf{r}}_i) + e_2^2(\hat{\mathbf{r}}_i)), \quad (37)$$

where n is the number of galaxies in a cell and σ_γ^2 is the predicted shear variance for square cells which we calculate for a Λ CDM model using $\sqrt{\pi} \times$ equation (26). Varying the cell side length yields the cell variance as a function of scale, $\sigma_{\text{lens}}^2(\theta)$. The error in equation (35) is given by

$$\text{Var}[\sigma_{\text{lens}}^2] = \frac{1}{\sum_{\text{cell}} w_{\text{cell}}}. \quad (38)$$

In Fig. 13, we plot our shear variance measurements along with the predicted shear variance signal for a Λ CDM model, and for three values of the power spectrum normalisation, $\sigma_8 = 0.8, 0.9$ & 1.0 . Immediately, one sees that the shear variance statistic is measuring a somewhat higher signal than the correlation function on scales $\lesssim 2$ arcmin. We suspect that this is the same effect as that seen in the correlation functions at very small scales, i.e. that at these scales residual systematics and/or intrinsic galaxy alignments become important. Very recently, methods have been developed for separating the intrinsic and lensing signals (Heymans & Heavens 2003; King & Schneider 2002) by effectively down-weighting physically close pairs of galaxies when calculating the correlation functions. Such methods are dependent on accurate photometric information being available for the individual galaxies. In this respect, the COMBO-17 survey is ideal for the separation of the intrinsic and lensing signals, and we are currently applying such an analysis to the survey. We note, for the purposes of the current lensing analysis, however, that intrinsic alignments are unlikely to contribute significantly to our signal beyond scales of a few arcmin in the shear variance or beyond ~ 1 arcmin in the correlation functions. Indeed, the few observational studies of intrinsic alignments carried out to date (Pen, Lee & Seljak 2000; Brown et al. 2002; Lee & Pen 2002) support arguments from both theoretical considerations (Crittenden et al. 2001; Catelan et al. 2001; Mackey et al. 2002) and numerical simulations (Heavens, Refregier & Heymans 2000; Croft & Metzler 2001) that predict the intrinsic contribution to be no more than $\sim 10\%$ for deep surveys such as COMBO-17. We do, however, urge caution when interpreting these statistics on scales $\lesssim 1$ arcmin.

6 COSMIC SHEAR LIKELIHOOD ANALYSIS

Having tested our data for sources of systematic errors and measuring the cosmic shear signal by standard methods, we now apply a new maximum likelihood analysis to estimate the cosmic shear

power spectrum from the COMBO-17 dataset. This section contains the key results of our paper.

6.1 Likelihood procedure

Our approach is based on the prescription of Hu & White (2001, hereafter HW), who use a maximum likelihood method to reconstruct the three power spectra, $C_\ell^{\kappa\kappa}$, $C_\ell^{\kappa\beta}$ and $C_\ell^{\beta\beta}$, directly from pixelised shear data. More precisely HW proposed reconstructing $C_\ell^{\kappa\kappa}$ as a series of step-wise ‘‘band powers’’, extracted from the data via an iterated quadratic estimator of the maximum likelihood solution. This approach, which is similar to methods used in analyses of CMB polarisation fields (e.g. Tegmark & de-Oliveira Costa 2002), has the advantage that it automatically accounts for irregular survey geometries and produces error estimates which include sampling variance and shot noise. In addition this approach can account for the effects of pixelisation.

HW have tested the maximum likelihood estimator on both Gaussian realisations of a Λ CDM power spectrum and on N-body simulations. In both cases, the estimator performs well, recovering the input power accurately with error estimates from the Fisher matrix showing excellent agreement with run-to-run errors. We also investigate the method with our own simulations in the next section.

Another advantage of this approach for reconstructing the shear power spectrum is that it provides a simple method for performing a decomposition of the signal into curl (β) and curl-free (κ) modes. The weak lensing shear power spectrum is predicted to be completely curl-free in the absence of significant lensing from gravitational waves (Stebbins 1997; Kamionkowski et al. 1998) although the predictions for intrinsic galaxy alignments are less certain (e.g. Crittenden et al. 2001, Mackey et al. 2002). The κ/β decomposition, therefore, represents a useful method for the detection of non-lensing artefacts (e.g. intrinsic alignments, systematic effects) in the data.

If we write our data as a vector,

$$\mathbf{d} = (\gamma_1(\hat{\mathbf{r}}_1), \gamma_2(\hat{\mathbf{r}}_1), \dots, \gamma_1(\hat{\mathbf{r}}_n), \gamma_2(\hat{\mathbf{r}}_n)),$$

then the likelihood function is

$$-2 \ln L(\mathbf{C}|\mathbf{d}) = \mathbf{d}^t \mathbf{C}^{-1} \mathbf{d} + \text{Tr}[\ln \mathbf{C}], \quad (39)$$

where

$$\mathbf{C} = \langle \mathbf{d} \mathbf{d}^t \rangle \quad (40)$$

is the data covariance matrix, and we assume uniform priors. We can interpret the data covariance matrix as the sum of the shear covariance matrix (equation (21)) and a noise term

$$\mathbf{N} = \frac{\gamma_{\text{rms}}^2}{N_{\text{pix}}} \mathbf{I}, \quad (41)$$

which we measure directly from the data. Here, \mathbf{I} is the identity matrix, γ_{rms} is the intrinsic dispersion of galaxy ellipticities within a pixel and N_{pix} is the pixel occupation number.

Following HW, we maximise the likelihood as a function of the model parameters. Here, our model parameters are just the band powers of the three power spectra, $C_\ell^{\kappa\kappa}$, $C_\ell^{\beta\beta}$ and $C_\ell^{\kappa\beta}$ and we perform the maximization iteratively with a Newton-Raphson scheme. That is, from an initial guess of the band powers, θ_i , a new estimate,

$$\theta_i' = \theta_i + \Delta\theta_i \quad (42)$$

is made for the band powers where we have adjusted our previous estimate by

$$\Delta\theta_j = 2 \left(\frac{\partial \ln L}{\partial \theta_i} \right) \left(\frac{\partial^2 \ln L}{\partial \theta_i \partial \theta_j} \right)^{-1}. \quad (43)$$

Here, we can replace the second derivative of the likelihood by its expectation value,

$$\left\langle \left(\frac{\partial^2 \ln L}{\partial \theta_i \partial \theta_j} \right)^{-1} \right\rangle \approx F_{ij}^{-1}, \quad (44)$$

and at the same time, in the limit where the likelihood is sufficiently Gaussian in the parameters, we can use the Fisher Information matrix (e.g. Tegmark, Taylor & Heavens 1997),

$$F_{ij} = \frac{1}{2} \text{Tr} [C^{-1} \partial_{\theta_i} C] \cdot [C^{-1} \partial_{\theta_j} C] \quad (45)$$

to estimate the uncertainties on the band power measurements. That is, we approximate the covariance matrix of our band power estimates as

$$\text{cov}[\theta_i, \theta_j] \approx F_{ij}^{-1}. \quad (46)$$

6.2 Testing the likelihood on simulations

Although HW test the likelihood reconstruction of the various power spectra on both Gaussian and N-body simulations, we have also conducted our own simulations of the likelihood reconstruction. We do this because of the small size of our data fields (30×30 arcmin) relative to HW's simulated fields, which are about 50 times larger in area.

We have applied the maximum likelihood estimator to one hundred 30×30 arcmin fields where the pixelised shear distribution in each field is a Gaussian realisation of a shear power spectrum calculated for a Λ CDM cosmology and for all source galaxies lying at $z = 1$. Following HW's approach, we have added Gaussian distributed noise to each of the 20×20 pixels (pixel size, 1.5×1.5 arcmin) of our shear distribution according to equation (41) where we have taken $\gamma_{\text{rms}} = 0.4$ for the intrinsic dispersion in galaxy ellipticity components. For the number of galaxies in each cell, we employ a mean galaxy density of $\bar{n}_g = 32.0 \text{ arcmin}^{-2}$, similar to the measured galaxy density of our dataset (see Table 1), and we calculate the pixel occupation number with $N_{\text{pix}} = \bar{n}_g \theta_{\text{pix}}^2$ where θ_{pix} is the pixel side length in arcmin. The results from all the simulations are summarised in Fig. 14 where we plot the recovered band powers of the three power spectra, $C_\ell^{\kappa\kappa}$, $C_\ell^{\beta\beta}$ and $C_\ell^{\kappa\beta}$, averaged over all simulation runs. Here, we plot both the run-to-run errors and the errors as estimated from the Fisher matrix which agree well with one another, supporting the use of the Fisher matrix to estimate errors on the band power measurements. We see from these simulation results that the maximum likelihood reconstruction recovers the input power very accurately for Fourier modes in the range $1000 \lesssim \ell \lesssim 5000$. There is some indication from the simulations, however, that the method may slightly over-estimate the power for ℓ -modes outside this range. However, this discrepancy is much smaller than the precision to which we measure the signal. Finally, we note that the likelihood reconstruction estimates of the β -mode power spectrum, $C_\ell^{\beta\beta}$ and the cross-correlation, $C_\ell^{\kappa\beta}$ are both consistent with zero on all scales, as expected for the input Gaussian shear model used to create the shear distributions.

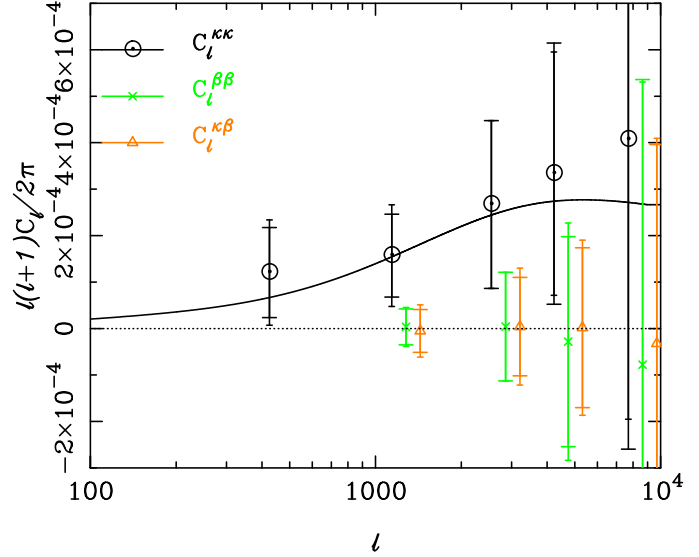


Figure 14. The recovered band powers of the three spectra, $C_\ell^{\kappa\kappa}$, $C_\ell^{\beta\beta}$ and $C_\ell^{\kappa\beta}$ as averaged over 100 Gaussian realisations. Error bars are shown as calculated from the run-to-run variations (smaller terminal ends) and also as estimated from the Fisher matrix (larger terminal ends). The solid curve is the input Λ CDM power spectrum used to create the simulated shear distributions. The $C_\ell^{\beta\beta}$ and $C_\ell^{\kappa\beta}$ points have been slightly offset horizontally for clarity.

6.3 Maximum likelihood results

6.3.1 Shear power spectra

Having tested the method on simulations, we now apply the maximum likelihood reconstruction to our five data fields, CDFS, SGP, FDF, S11 and A901/2. As these fields are widely separated on the sky we can treat them as independent and optimally combine them afterwards.

Fig. 15 shows the results of estimating $C_\ell^{\kappa\kappa}$, $C_\ell^{\kappa\beta}$ and $C_\ell^{\beta\beta}$ for the five fields, in 5 band powers. Also plotted is a model curve for the Λ CDM model with $\Omega_\Lambda = 0.7$, $\Omega_m = 0.3$, $h = 0.68$, normalised to $\sigma_8 = 0.8$ (see Section 7). The linear power spectrum has been transformed to a nonlinear one using the halo fit formulae of Smith et al. (2002) and, again, we have included the composite redshift distribution shown in Fig. 8 in this calculation.

In general we find that the fields containing clusters, S11 and A901/2, both yield higher results than the other fields. However, as mentioned already, the results for the S11 field seem consistent with the dataset as a whole while those for the A901/2 field clearly are not. That the shape is broadly the same for the A901 field is to be expected since this part of the nonlinear power spectrum is dominated by massive clusters (Cooray & Hu 2001). At the median redshift of the sample, the peak of the nonlinear convergence power spectrum corresponds to around $3h^{-1}\text{Mpc}$, the scale on which we expect collapsed clusters to have virialised.

The other fields, CDFS, the SGP and FDF, are fields without large structures and have correspondingly lower amplitude spectra. Interestingly on the smallest scales, $\ell \approx 4000$, the power is roughly the same in all five fields.

Fig. 16 shows the power from an optimal inverse weighting combination of the fields excluding A901/2. Details of the opti-

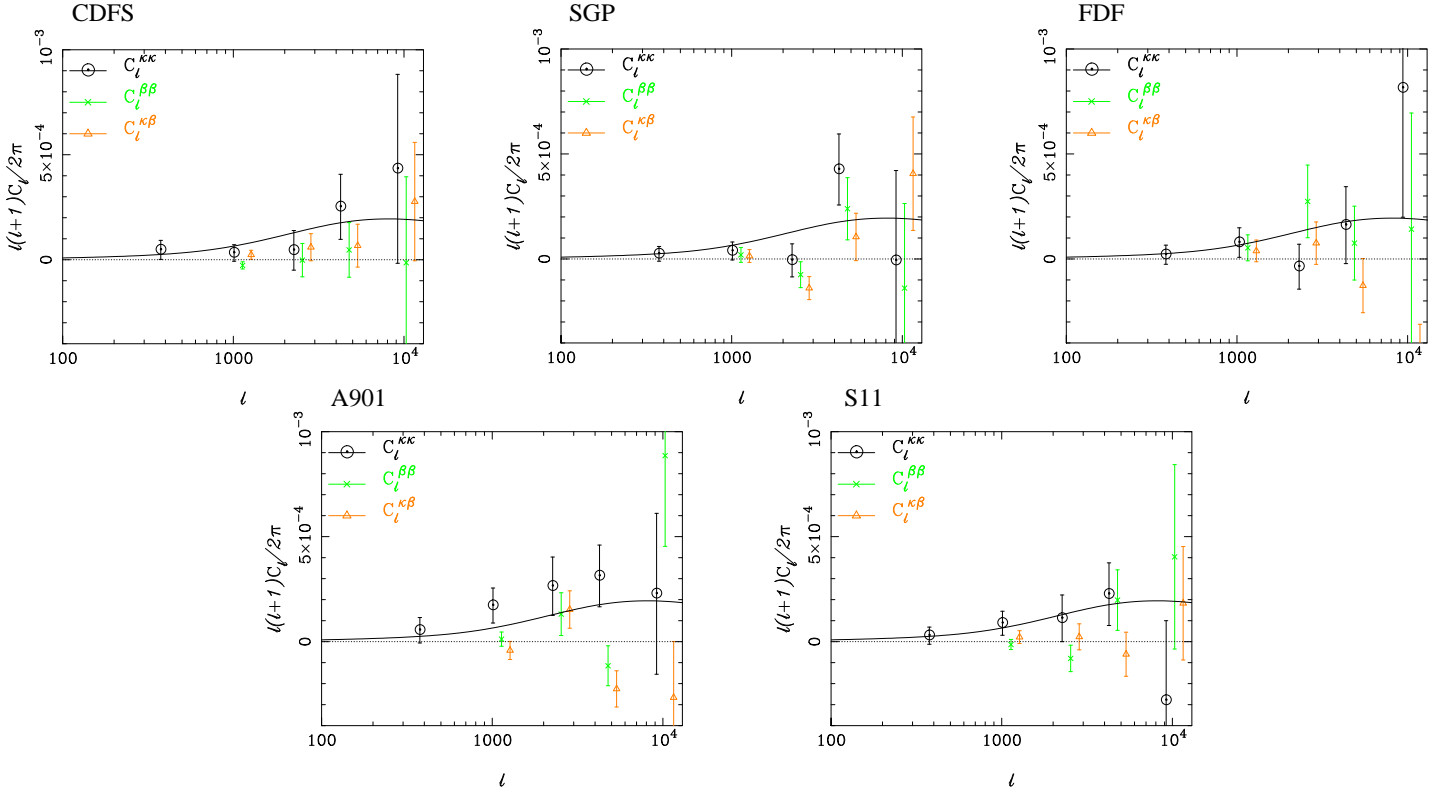


Figure 15. The cosmic shear power spectra estimated from each of the five individual fields in the COMBO-17 dataset. The spectra are for (clockwise, from top left) CDFS, SGP, FDF, S11 and A901. Note the much higher power recovered from the A901 supercluster field. The $C_\ell^{\beta\beta}$ and $C_\ell^{\kappa\beta}$ points have been slightly offset horizontally for clarity.

mally combined power spectra measurements are also given in Table 3. Three of our five band power measurements agree within their error bars with the $\sigma_8 = 0.8$ normalised Λ CDM model plotted. The high level of power measured at $\ell \sim 4000$ seems to be present in each of the fields we have analysed. The largest discrepancy between the model and the measurements occurs at $\ell = 2000$ where less than half the power is found.

In order to interpret the scales that we are probing with our power spectrum measurements, we note that, in a flat cosmology, the angular size will scale roughly as

$$R \simeq \frac{2\pi D_A}{\ell}, \quad (47)$$

where, for a flat Λ CDM Universe, the angular diameter distance (D_A) is well approximated by (Broadhurst, Taylor & Peacock 1995)

$$D_A(z) \simeq \frac{c}{H_0} \frac{z}{(1+z)(1+3/4\Omega_m z)}. \quad (48)$$

An estimate for the redshift of typical deflectors in the survey is $z_d \approx 0.5z_m$ and we have estimated $z_m \sim 0.85$ (see Section 4.1) for the median redshift of our survey. Combining these relations (with $\Omega_m = 0.3$) gives the following approximate conversion between the physical scale being probed and the Fourier variable on the sky:

$$R \simeq \frac{5130}{\ell} h^{-1} \text{Mpc}. \quad (49)$$

This relation gives the approximate physical scale indicated at the top of Fig. 16.

We can check our results for systematic effects by estimating the power in the β - β modes, as well as the κ - β cross correlation.

Table 3. Details of the maximum likelihood reconstructed band powers as obtained from the optimal combination of the four fields, CDFS, S11, SGP and FDF. The first two columns list the ℓ -range of the five band powers. Also listed are the detections and uncertainties in each band where we quote the band powers, $P_{ii} = \ell(\ell+1)C_\ell^{ii}/2\pi$ for $i = \kappa, \beta$. The first band only has $P_{\kappa\kappa}$ measurements as the κ and β powers are essentially indistinguishable at these large scales.

ℓ_{\min}	ℓ_{\max}	$P_{\kappa\kappa}(\times 10^5)$	$P_{\beta\beta}(\times 10^5)$	$P_{\kappa\beta}(\times 10^5)$
247	594	2.92 ± 2.05	–	–
595	1790	4.95 ± 2.43	-1.45 ± 1.26	2.21 ± 1.45
1791	2986	2.20 ± 4.75	-4.38 ± 3.76	-1.99 ± 3.27
2987	6324	26.62 ± 8.12	13.85 ± 7.34	0.49 ± 5.54
6325	13906	11.57 ± 22.39	7.87 ± 22.03	14.83 ± 14.64

In all of our band powers the β - β correlation is below the detected signal in κ and is consistent with zero in all but one band power at $\ell \sim 4000$. Similarly the κ - β cross correlation is well below our measurement of shear power, and is consistent with zero except at $\ell \sim 1000$ where a significant detection appears. We conclude from the minimal power found in these spectra that our results are not strongly contaminated by systematic effects.

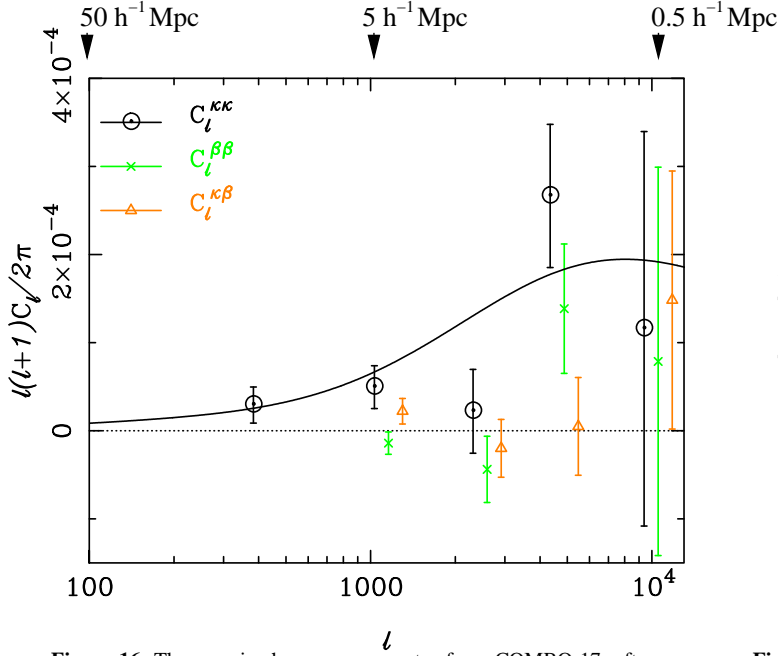


Figure 16. The cosmic shear power spectra from COMBO-17, after excluding the A901 supercluster field. Plotted on a linear-log scale are $C_\ell^{\kappa\kappa}$ (circles), $C_\ell^{\beta\beta}$ (crosses) and $C_\ell^{\kappa\beta}$ (triangles) in 5 band-averaged band powers, as a function of multipole, ℓ , estimated from the optimal combination of a maximum likelihood analysis of the four COMBO-17 fields, CDFS, SGP, FDF, and S11. The error bars are estimated from the Fisher matrix. The solid curve is the shear power spectrum expected for a $\sigma_8 = 0.8$ normalised Λ CDM model. Once again, the $C_\ell^{\beta\beta}$ and $C_\ell^{\kappa\beta}$ points have been slightly horizontally displaced for clarity.

6.3.2 Covariance matrix of band powers

In addition to measuring the amplitude of the shear power spectrum, it is also important to consider the correlations between band powers. We can quantify how much the bands are correlated with one another with the correlation matrix, defined by

$$\text{Cor}_{ij} = \frac{\text{Cov}_{ij}}{\sqrt{\text{Cov}_{ii}\text{Cov}_{jj}}}, \quad (50)$$

where Cov_{ij} is the covariance matrix of the band powers, which we measure directly from the data. In Fig. 17, we plot the correlation matrix of the optimally combined band power measurements shown in Fig. 16. It is clear from this figure that our band power measurements show very little correlation with one another, the biggest effect being the slight anti-correlation of neighbouring bands. Thus, our maximum likelihood band powers are almost independent measures of power.

6.4 Integral power spectra approximations

As well as a maximum likelihood approach, more direct methods have been proposed for recovering the shear power spectra. We have applied one of these direct methods, proposed by Schneider et al. (2002, hereafter SvWKM), to our data. SvWKM proposed reconstructing $C_\ell^{\kappa\kappa}$ directly from a correlation function analysis of the data, via an inversion of equation (25). Pen et al. (2002) have also suggested a similar approach, but with a somewhat different implementation, which they apply to the DESCART dataset.

The correlation function estimator, which can also be formulated in terms of band powers, is not dependent on the spatial

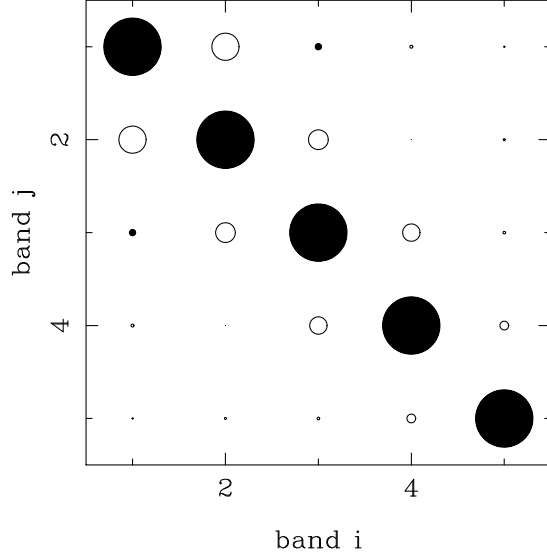


Figure 17. The correlation matrix (see text for details) of the optimally combined band power measurements recovered from the maximum likelihood reconstruction of $C_\ell^{\kappa\kappa}$. The area of each circle is proportional to the degree of correlation between bands i and j . Filled circles denote that the bands are correlated whereas unfilled circles denote an anti-correlation between the bands. The bands are the same as those plotted in Fig. 16, numbered 1 to 5, in order from left to right. Note the small values of the off-diagonal elements, indicating small (anti-)correlations between different band power measurements.

distribution of the shear and, as pointed out by SvWKM should not suffer from bleeding of power between bands due to pixelisation of the data. SvWKM test their estimator by reconstructing the power spectrum from a fiducial weak lensing survey of area, $A=25 \text{ deg}^2$ from which they assume they have measured the correlation functions for $6'' \leq \theta \leq 2^\circ$. For such a survey, the estimator recovers the input power very accurately for ℓ -modes in the range $200 \lesssim \ell \lesssim 2 \times 10^5$ and SvWKM also measure minimal covariance between their band powers over this range. Over the range, $2\pi/\theta_{\text{max}} \lesssim \ell \lesssim 2\pi/\theta_{\text{min}}$, the correlation function estimator is practically unbiased where $\theta_{\text{min}}(\theta_{\text{max}})$ is the smallest (largest) scale at which the correlation functions have been measured. Here we apply a modified version of the SvWKM statistic to our dataset. If we define two new correlation functions, $\xi_+(\theta) = C_1(\theta) + C_2(\theta)$ and $\xi_-(\theta) = C_1(\theta) - C_2(\theta)$, the correlation function estimator of SvWKM can be written as

$$C_\ell = 2\pi \int_{\theta_{\text{min}}}^{\theta_{\text{max}}} d\theta [K_1 \xi_+(\theta) J_0(\ell\theta) + K_2 \xi_-(\theta) J_4(\ell\theta)], \quad (51)$$

where $J_{0,4}(\ell\theta)$ are the usual Bessel functions and K_1 & K_2 describe the relative contribution from the $\xi_{+,-}(\theta)$ correlators to the integral. In order to achieve an optimal combination of ξ_+ and ξ_- contributions to the integral, SvWKM have constructed a function, $K_1(\ell)$ and imposed the constraint, $K_2 = 1 - K_1(\ell)$. However, in order to decompose our signal into κ and β modes, we have chosen K_1 and K_2 to be constants, independent of ℓ . Setting $K_1 = K_2 = 1/2$ yields a purely κ -mode estimator, whereas if we set $K_1 = 1/2$ and $K_2 = -1/2$, the estimator should recover only the β -mode power. Following SvWKM, we have formulated the correlation function estimator in terms of band powers.

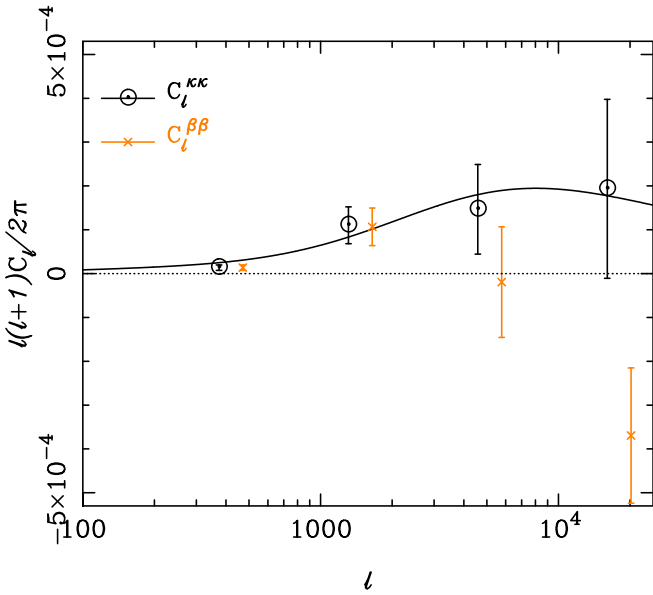


Figure 18. The shear power spectrum, $C_\ell^{\kappa\kappa}$ and the β -mode spectrum, $C_\ell^{\beta\beta}$ as estimated via a modified version (see text for details) of SvWKM’s correlation function estimator. The $C_\ell^{\beta\beta}$ points have been laterally displaced for clarity. Again, we have excluded the A901 supercluster field for these measurements. Also shown is the shear power spectrum expected for a $\sigma_8 = 0.8$ normalised Λ CDM model.

Fig. 18 shows the result of applying the correlation function estimator to COMBO-17. Again, we have excluded the A901 supercluster field from this calculation. We note that only the third band power on this plot is within the stated range of validity of the SvWKM estimator. Indeed, this data point is in good agreement with the $\Omega_m = 0.3$ Λ CDM model plotted and the power in β for this band power is consistent with zero. On both larger and smaller scales however, as predicted by SvWKM, the estimates becomes unreliable, measuring equal κ and β modes on large scales. Ideally, of course, one would measure the correlation functions out to as large a scale as possible to extend the range of applicability of the estimator. However, for our dataset, we only have correlation function measurements in the range $20'' \lesssim \theta \lesssim 12'$ giving us a valid ℓ -range of $1800 \lesssim \ell \lesssim 5000$. We conclude, therefore, that although reconstructing the shear power spectrum from a correlation function analysis can be useful for datasets with larger fields, for our purposes, the full maximum likelihood analysis is clearly the most suitable approach.

7 COSMOLOGICAL PARAMETER ESTIMATION

7.1 Ω_m and σ_8 from COMBO-17

Having measured various statistics from the data, we are now in a position to use both our measured shear correlation functions and our reconstructed shear power spectrum estimates to obtain a joint measurement of the normalisation of the mass power spectrum σ_8 , and the matter density Ω_m . We can achieve this by fitting theoretical shear correlation functions and power spectra, calculated for particular values of these parameters, to our measurements.

Again, we use the fitting functions of Smith et al. (2002) to produce dark matter power spectra $P_\delta(k, r)$ for values of σ_8 ranging from 0.1 to 1.5 and Ω_m from 0.1 to 1.0, exploring all values

on a grid with 0.01 spacing in these parameters. We choose to fix $\Omega_m + \Omega_\Lambda = 1$. For all our theoretical power spectra and correlation functions, we use $H_0 = 100h = 68 \text{ km s}^{-1} \text{ Mpc}^{-1}$ for the value of the Hubble constant and $n = 1$ for the initial slope of the power spectrum of density fluctuations. For each set of parameters, we calculate the corresponding shear power spectrum using equation (17). Note that we input our composite redshift distribution (Fig. 8) into the calculation for the shear power spectra. Having calculated the shear power spectra we obtain the correlation functions $C_{1,2}$ using equation (25).

We fit the above models to our correlation function and shear power spectrum data (where the A901 supercluster field has been excluded in both cases) using a χ^2 fitting procedure (c.f. Bacon et al. 2002). We order our correlation function measurements as a vector $\mathbf{d} \equiv \{C_1(\theta_n), C_2(\theta_n)\}$, where $C_{1,2}(\theta_n)$ is the mean correlation function (averaged over all sections) for a given angular separation (see Section 5.1). Similarly, we order our theoretical correlation functions as vectors $\mathbf{x}(a)$ with the same format, where $a = (\sigma_8, \Omega_m)$.

We use the log-likelihood estimator

$$\chi^2 = [\mathbf{d} - \mathbf{x}(a)]^T \mathbf{V}^{-1} [\mathbf{d} - \mathbf{x}(a)], \quad (52)$$

where

$$\mathbf{V} = \langle \mathbf{d} \mathbf{d}^t \rangle \quad (53)$$

is the covariance matrix of our correlation function measurements, which we measure directly from our data using equation (33). This estimator is valid in the case of Gaussian errors, which we achieve since we have averaged over many sections. We calculate χ^2 for our fine grid of (σ_8, Ω_m) theoretical correlation functions, and find the minimum and confidence intervals.

The χ^2 fitting for the shear power spectrum measurements is done in exactly the same way as for the correlation function analysis.

7.1.1 Correlation function results

For the correlation function analysis, we find a best fit $\sigma_8(\Omega_m/0.3)^{0.52} = 0.75$, with reduced χ^2 of 1.21. The 1σ error bar on this value, for a 1 parameter fit, is given by the boundary $\Delta\chi^2 = 1.0$, which occurs here at $\sigma_8 = 0.81$ and 0.69. To date, one of the biggest sources of error in cosmic shear measurements of cosmological parameters has been the uncertainty in the median redshift of the source galaxies. The cosmic shear signal scales as $\sigma_\gamma^2 \propto \sigma_8^{2.5} z^{1.6}$ (see e.g. BRE). So the uncertainty in the median redshift contributes to the error in σ_8 as

$$\left(\frac{\delta\sigma'_8}{\sigma'_8}\right)^2 = \left(\frac{\delta\sigma_8}{\sigma_8}\right)^2 + 0.64^2 \left(\frac{\delta z}{z}\right)^2. \quad (54)$$

Using our estimate of the median redshift of the COMBO-17 galaxies, $z_m = 0.85 \pm 0.05$ (see Section 4.2), we have investigated the extra uncertainty introduced into our measurement of σ_8 by equation (54). We find the additional error introduced due to the median redshift uncertainty to be 0.01. Thus we obtain a measurement signal-to-noise of ~ 9 for the amplitude of the power spectrum, with a measurement of the amplitude

$$\sigma_8(\Omega_m/0.3)^{0.52} = 0.75^{+0.08}_{-0.08}. \quad (55)$$

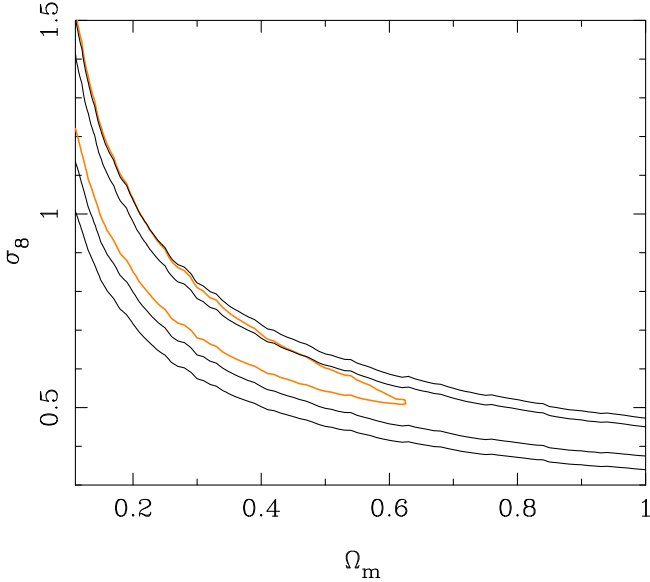


Figure 19. The likelihood surface of σ_8 and Ω_m from COMBO-17 as calculated using our correlation function measurements (lighter contour) and as calculated using our shear power spectrum measurements (dark contours). For the power spectra measurements we plot the 1 and 2 σ contours. For the correlation functions, we plot only the 1 σ contour for clarity.

7.1.2 Shear power spectrum results

The results for the shear power spectrum analysis yield a slightly lower amplitude for the power spectrum normalisation. A good fit to the parameter constraints as calculated using our shear power spectrum measurements is $\sigma_8(\Omega_m/0.3)^{0.49} = 0.72$, with a reduced χ^2 of 2.21. The additional error due to the uncertainty in z_s is again 0.01. Our final measurement for the normalisation of the mass power spectrum, as calculated from our shear power spectrum measurements is

$$\sigma_8(\Omega_m/0.3)^{0.49} = 0.72_{-0.09}^{+0.08}. \quad (56)$$

These constraints, as calculated using both of our methods are shown as contours in the $\sigma_8 - \Omega_m$ plane in Fig. 19. Note that in the case of the correlation function constraints, values of $\Omega_m \gtrsim 0.63$ are excluded at the 1 σ level.

7.2 Including the actual redshift distribution

In order to demonstrate the power of accurate redshift information we have also measured parameters from correlation functions which have been calculated using only galaxies with reliable redshift estimates. In this case, for our theoretical curves, we input the *actual* redshift distribution of the lensed source galaxies (i.e. the dotted curve in Fig. 8). For the purposes of this demonstrative calculation, we have included the A901/2 supercluster field. We do this simply to increase the number of galaxies – at present, photometric redshifts are only available for the CDFS, S11 and A901 fields and there were too few galaxies with reliable redshifts in CDFS and S11 alone (19143 galaxies) to constrain parameters significantly. Adding the 12506 galaxies with accurate redshifts in the A901 field to this sample enabled us to obtain reasonable constraints on Ω_m and σ_8 . The result, therefore, will clearly be biased

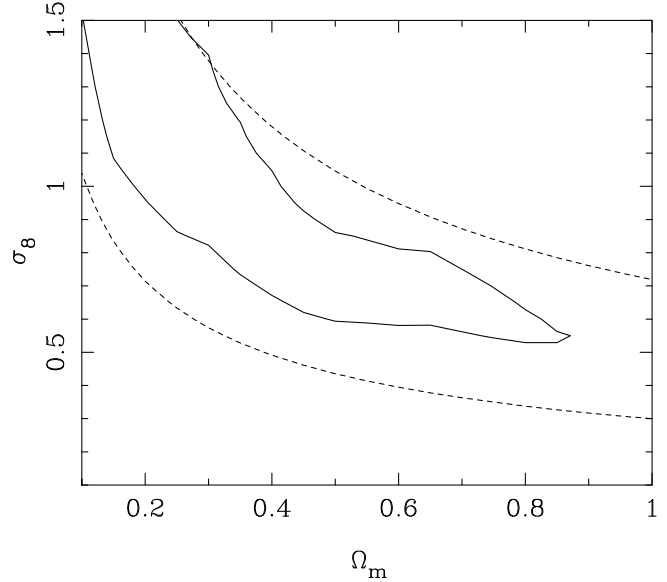


Figure 20. The likelihood surface of σ_8 and Ω_m from COMBO-17 using correlation functions measured only from galaxies with accurate redshift estimates. This subset of galaxies only includes galaxies in the CDFS, S11 and A901 fields with R-band magnitudes ≤ 24.0 . The 1 σ contour is plotted as a full line. For comparison, we also plot the 1 σ confidence region (dashed contour) obtained from the same correlation functions excluding the redshift information. For this calculation the only redshift information we assume is an estimate of the median redshift of the survey ($z_m = 0.6 \pm 0.2$).

by the A901/2 field and cannot be taken as a measure of the power spectrum amplitude. However, it does dramatically demonstrate the increase in accuracy attainable with accurate photometric information.

The results are shown in Fig. 20. For comparison, we also plot the constraints obtained from the same set of correlation function measurements where we have assumed a median redshift and uncertainty of $z_m = 0.6 \pm 0.2$. Here, $z_m = 0.6$ is the measured median redshift of galaxies with reliable assigned redshifts in the COMBO-17 survey and $\Delta z = 0.2$ is typical of the estimated uncertainty in the median redshift of cosmic shear surveys to date. In agreement with the shear power spectrum analysis (see section 6.3), we see the effect of the A901 supercluster pushing the best-fit σ_8 value up to ~ 1 for a matter density of $\Omega_m = 0.3$. Once again, we emphasise that we are not presenting this as a measurement of σ_8 – we simply wish to demonstrate the dramatic improvement in parameter constraints obtainable with the inclusion of accurate photometric information. Clearly for accurate parameter estimates, a greater understanding of the source redshift distribution must be a priority for cosmic shear surveys in the future.

7.3 Combination with the 2dFGRS and CMB experiments

We can combine the confidence region given by equation (56) or by Fig. 19, with parameter estimations from other sources such as the 2dF Galaxy Redshift Survey (2dFGRS, Percival et al. 2002) and the various CMB experiments (Lewis & Bridle 2002 & references therein).

In order to combine our measurements with those from the 2dFGRS and the CMB data, we first impose some priors on the various datasets. Firstly, we consider only flat Universe models

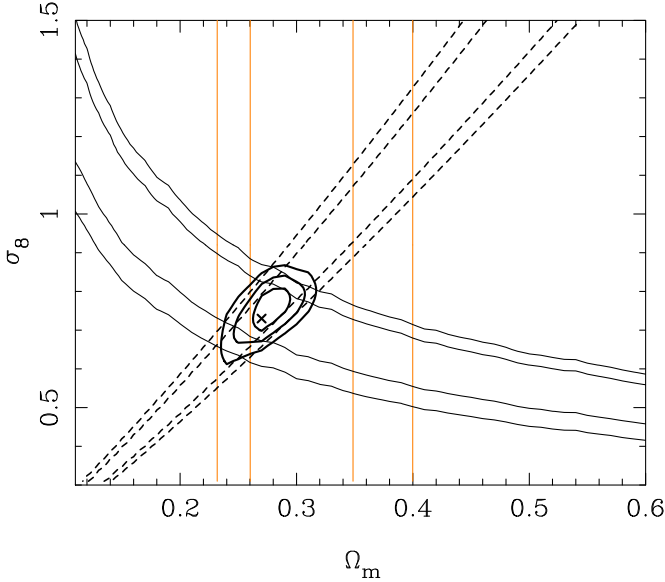


Figure 21. The likelihood surface of σ_8 and Ω_m from combining the COMBO-17 dataset with the 2dFGRS and the latest CMB constraints. The dark thin solid contours are the constraints obtained from our shear power spectrum analysis described in the previous section. The lighter vertical contours are the constraints on Ω_m obtained from the 2dFGRS where we have applied the priors described in the text to the 2dF data. The dashed set of contours are the constraints from a compilation of six CMB experiments (see text for details) where we have assumed an optical depth to reionization of $\tau = 0.10$. The dark heavy contours are the 1,2 and 3 σ combined constraints from the three methods. The best fit values of Ω_m and σ_8 are also indicated.

($\Omega_\Lambda + \Omega_m = 1$) as compelling evidence for a flat Universe has already been found from the CMB data (e.g. de Bernardis et al. 2002; Pryke et al. 2002; Lewis & Bridle 2002). For the slope of the power spectrum of the primordial density perturbations, we take $n_s = 1$ and for the baryon fraction $f_b = \Omega_b/\Omega_m$, we take $f_b = 0.16$. These values are consistent with those measured from joint analyses of CMB and Large Scale Structure (LSS) data (e.g. Efstathiou et al. 2001; Wang, Tegmark & Zaldarriaga 2002; Percival et al. 2002; Knox, Christensen & Skordis 2002). To display the additional constraints in the $\sigma_8 - \Omega_m$ plane, we also need to choose a value for the Hubble parameter, h . We have taken the value $h = 0.68$, found from a joint analysis of the CMB and 2dF data for a flat Universe and for a scalar-only spectral index, n_s (Percival et al. 2002; Efstathiou et al. 2002). Note that this is the same value of h which we adopted when making our model predictions in the previous section. Finally, we note that this value is consistent with the HST Key Project within the quoted errors (Freedman et al. 2001).

Having set these various parameters, in the case of the 2dFGRS, for each of our grid points in the (Ω_m, σ_8) plane, we simply add the corresponding likelihood values from Percival et al. (2002) to the likelihoods already obtained in the previous section from our shear power spectrum data. For the CMB constraints, we have adopted the results of Lewis & Bridle (2002) who provide the following joint constraint on Ω_m and σ_8 as found from a compilation of six CMB experiments:

$$\nu = \Omega_m h^{2.35} (\sigma_8 e^{-\tau}/0.7)^{-0.84} = 0.115 \pm 0.0047. \quad (57)$$

Here, τ is the optical depth to reionization. For each point on our (Ω_m, σ_8) grid, we calculate likelihoods for the CMB data as

$$\chi_{\text{CMB}}^2 = \frac{(\nu - \Omega_m h^{2.35} (\sigma_8 e^{-\tau}/0.7)^{-0.84})^2}{(\delta\nu)^2} \quad (58)$$

with $\nu = 0.115$, $\delta\nu = 0.0047$ and $h = 0.68$. Finally, we add the likelihoods from the various data to get our final measurements of Ω_m and σ_8 . The results of this combination are shown in Figure 21 for an optical depth of $\tau = 0.10$. Note that the 2dFGRS data we have used for this estimation constrains Ω_m only and so the constraints shown on σ_8 come wholly from the cosmic shear and CMB measurements. We measure best-fit values of $\Omega_m = 0.27^{+0.02}_{-0.01}$ and $\sigma_8 = 0.73^{+0.06}_{-0.03}$ from the combined data.

We have also investigated the effect a non-zero τ has on these measurements. We find that increasing/decreasing τ has the effect of increasing/decreasing the slope of the CMB constraints somewhat, but the resulting combined constraints are not altered drastically. For example, for an optical depth of $\tau = 0.00$, the best-fit Ω_m and σ_8 values change to 0.29 and 0.72 respectively, while increasing τ to 0.25 changes the best-fit values to $\Omega_m = 0.25$ and $\sigma_8 = 0.77$.

8 CONCLUSIONS

We have presented an analysis of the cosmic shear signal in the COMBO-17 survey, a 1.25 square degree survey with excellent data quality, including photometric redshifts for $\sim 38\%$ of our galaxy sample for three of the five $0.5^\circ \times 0.5^\circ$ fields. Our measurements follow a process of careful data reduction, assessment of the level of telescope-induced shear, and correction for PSF anisotropy and circularization of galaxies. In this fashion we reduce the residual systematic effects to a level $< 5\%$ of the cosmic shear signal.

We have measured shear correlation functions and variance-weighted shear cell-variance for our galaxy sample, detecting the cosmic shear signal at the 5 σ level. On scales $\gtrsim 1$ arcmin, where we are confident of the cosmological origin of the signal, we find a somewhat lower amplitude than other cosmic shear surveys have measured to date.

In contrast to previous cosmic shear surveys, we have substantially reduced the usual uncertainty introduced into the interpretation of cosmic shear measurements due to a lack of knowledge of the redshift distribution. We have done this by estimating from the data the median redshift of the lensed source galaxies to be $z_m = 0.85 \pm 0.05$.

We have used our catalogues of galaxy positions and shear estimates to apply a maximum likelihood analysis, obtaining the shear power spectrum for each COMBO-17 field and for the entire survey. We have measured the κ -field power spectrum expected to arise from gravitational shear, from $\ell = 400$ to 10^4 , and have shown that the systematically-induced β -field power spectrum is substantially below our shear signal throughout this ℓ range. We find that the power spectrum for a supercluster field has a significantly higher amplitude than that for random fields, as expected, and we have therefore excluded this field from our final optimally combined result. Simulations of the maximum likelihood procedure demonstrate that our method is unbiased to within $\sim 10\%$. We have measured the covariance matrix of our shear power spectrum band powers directly from the data and find our band powers to be essentially independent measured of power.

We have also investigated the use of correlation function estimators (e.g. SvWKM) for the shear power spectrum and find, in

agreement with SvWKM, that their success is dependent on the correlation functions being measured over a large range of scales. Such estimators are therefore difficult to apply to datasets composed of small fields.

We have used our shear correlation function and power spectrum measurements to estimate constraints on the cosmological parameters Ω_m and σ_8 . We have made χ^2 fits of our measurements to predicted functions for various values of these cosmological parameters, and we measure the amplitude of the mass power spectrum, from our shear power spectrum results to be $\sigma_8 \left(\frac{\Omega_m}{0.3}\right)^{0.49} = 0.72 \pm 0.09$ with $0.10 < \Omega_m < 0.63$, including uncertainties due to statistical noise, sample variance, and redshift distribution.

We have demonstrated the potential of including photometric redshift information by constraining these cosmological parameters with only those galaxies with assigned redshifts. For this calculation, we have input the actual measured redshift distribution into the theoretical predictions and have compared the resulting constraints with those that would be obtained with only an estimate of the median redshift of the survey. We thus demonstrate the dramatic increase in precision obtained by including accurate redshift information for the source galaxy distribution.

We have combined our constraints with those from the 2dF Galaxy Redshift Survey, and the latest CMB experiments, finding a power spectrum normalisation of $\sigma_8 = 0.73^{+0.06}_{-0.03}$ and a matter density of $\Omega_m = 0.27^{+0.02}_{-0.01}$.

These results (for both the lensing alone, and for the combined constraints) are lower than previous constraints found from cosmic shear surveys (e.g. Bacon et al. 2002, Refregier et al. 2002, Van Waerbeke et al. 2002, Hoekstra et al. 2002) which have, until now found power spectrum normalisations of $\sigma_8 \sim 0.85 - 1.0$. However, our measurements are much more in agreement with recent cluster abundance estimates of the power spectrum normalisation (Borgani et al 2001; Seljak 2002; Reiprich & Böhringer 2002; Viana, Nichol & Liddle 2002, Allen et al. 2002; Schuecker et al. 2003, Pierpaoli et al. 2002) and those found from combining constraints from the 2dFGRS and CMB results (e.g. Lahav et al. 2001, Melchiorri & Silk 2002). Finally, we note that our results agree within the 2σ level with recently announced results from the WMAP satellite (Spergel et al. 2003).

Since this paper was submitted, two other groups have presented cosmic shear results yielding somewhat lower values of σ_8 – Jarvis et al. 2003 measure the shear signal from the 75 sq. degree CTIO survey and find a power spectrum normalisation of $\sigma_8 = 0.71$ while Hamana et al. 2002 have used the Suprime-Cam instrument on the Subaru telescope to measure the cosmic shear signal from 2.1 sq. degs. of deep *R* band data, with which they constrain the power spectrum normalisation to be $\sigma_8 = 0.69$. The results from both these studies are in excellent agreement with the results presented here.

We have tested our dataset extensively for systematic effects by measuring galaxy cross-correlations, star-galaxy correlations and by decomposing the cosmic shear signal into its constituent curl and curl-free modes. However, we have found our dataset to be largely free of any systematic effect that could account for the discrepancy found between our parameter constraints and those obtained from previous weak lensing studies. One factor, which must be important, is the increased understanding of the source redshift distribution which we have gained from the 17-band photometric information contained in the COMBO-17 survey. With the increase in area of cosmic shear surveys in the future, this type of redshift information is likely to become vital as the uncertainties due to the

redshift distribution become dominant over other sources of error such as shot noise and sampling variance.

ACKNOWLEDGEMENTS

MLB thanks the University of Edinburgh for a studentship. ANT thanks the PPARC for an Advanced Fellowship and DJB and MEG are supported by PPARC Postdoctoral Fellowships. SD thanks the PPARC for a PDRA grant. CW thanks the PPARC for a PDRA position from the rolling grant in observational cosmology at Oxford. We also thank Wayne Hu and Martin White for making their original likelihood code available, which we adapted to carry out the analysis in Section 6. We are grateful to Will Percival for providing us with the 2dFGRS data used in Section 7 and we thank Nigel Hambly for providing the SuperCOSMOS data for our astrometric calibrations. We thank Peter Schneider, Martin White & Wayne Hu for helpful comments on an earlier draft of the paper. Finally, we thank Alan Heavens, Will Percival and Ali Higgins for useful discussions.

REFERENCES

- Allen S. W., Fabian A. C., Schmidt R. W., Ebeling H., 2002, MNRAS, accepted (astro-ph 0208394)
- Bacon D. J., Massey R. J., Refregier A., Ellis R., 2002, MNRAS, submitted (astro-ph 0203134)
- Bacon D. J., Refregier A., Ellis R., 2000, MNRAS, 318, 625 (BRE)
- Bacon D. J., Taylor A. N., 2002, MNRAS, submitted (astro-ph/0212266)
- Barber A., 2002, MNRAS, 335, 909
- Bartelmann M., Narayan, R., 1995, ApJ, 451, 60
- Bartelmann M., Schneider, P., 2001, Physics Reports, 340, 291
- Baugh C. M., Efstathiou G., 1991, MNRAS, 265, 145
- Bernardeau F., Van Waerbeke L., Mellier Y., 1997, A&A, 322, 1
- Bernstein G., Jarvis M., 2002, AJ, 123, 583
- Bertin E., Arnouts S., 1996, A&AS, 117, 393
- Borgani S. et al., 2001, ApJ, 561, 13
- Broadhurst T. J., Taylor A. N., Peacock J. A., 1995, MNRAS, 299, 895
- Brown M. L., Taylor A. N., Hambly N. C., Dye S., 2002, MNRAS, 333, 501
- Bunn E., 2002, Phys. Rev. D., 65, 4
- Catelan P., Kamionkowski M., Blandford R. D., 2001, MNRAS, 323, 713
- Cohen J. G., Hogg D. W., Blandford R., Cowie L. L., Hu. E., Songaila A., Shopbell P., Richberg K., 2000, ApJ, 538, 29
- Cooray A., Hu W., 2001, ApJ, 554, 56
- Crittenden R., Natarajan P., Pen U., Theuns, T., 2001, ApJ, 545, 561
- Croft. R. A. C., Metzler C. A., 2001, ApJ, 545, 561
- de Bernardis P. et al., 2002, ApJ, 564, 559
- Efstathiou G. et al., 2002, MNRAS, 330, L29
- Freedman W. L. et al., 2001, ApJ, 553, 47
- Gray M. E., Taylor A. N., Meisenheimer K., Dye S., Wolf C., Thommes E., 2002, ApJ, 568, 141 (GTM+)
- Hamana T. et al., 2002, ApJ, submitted (astro-ph 0210450)
- Hambly N. et al., 2001, MNRAS, 326, 1279
- Heavens A. F., Refregier A., Heymans C., 2000, MNRAS, 319, 649
- Heymans C., Heavens A. F., 2003, MNRAS, 339, 711

- Hoekstra H., Franx M., Kuijken K., Squires G., 1998, *New Astronomy Review*, 42, 137
- Hoekstra H., Yee H. K. C., Gladders M. D., 2001, *ApJ*, 558, L11
- Hoekstra H., Yee H. K. C., Gladders M. D., Barrientos L. F., Hall P. B., Leopoldo I., 2002, *ApJ*, 572, 55
- Hu W., 2000, *Phys. Rev. D.*, 62, 3007
- Hu W., Keeton C. R., 2002, *Phys. Rev. D.*, 66, 063506
- Hu W., Tegmark M., 1999, *ApJ*, 514, L65
- Hu W., White M., 2001, *ApJ*, 554, 67 (HW)
- Jain B., Seljak U., 1997, *ApJ*, 484, 560
- Jarvis M., Bernstein G. M., Fischer P., Smith D., Jain B., Tyson J. A., Wittmann D., 2003, *AJ*, 125, 1014
- Kaiser N., 1998, *ApJ*, 498, 26
- Kaiser N., Squires G., 1993, *ApJ*, 404, 441
- Kaiser N., Squires G., Broadhurst T. J., 1995, *ApJ*, 449, 460 (KSB)
- Kaiser N., Wilson G. Luppino G., Dahle I., 1999, PASP submitted (astro-ph 9907229)
- Kamionkowski M., Babul A., Cress C. M., Refregier A., 1998, *MNRAS*, 301, 1064
- King L., Schneider P., 2002, *A&A*, 396, 411
- Knox L., Christensen N., Skordis C., 2002, *ApJ*, 563, L95
- Lahav O. et al., 2002, *MNRAS*, 333, 961
- Lee J., Pen U., 2002, *ApJ*, 567, L111
- Lewis A., Bridle S., 2002, *Phys. Rev. D.*, 66, 103511
- Luppino G. A., Kaiser N., 1997, *ApJ*, 475, 20
- Mackey J., White M., Kamionkowski M., 2002, *MNRAS*, 332, 788
- Melchiorri A., Silk, J., 2002, *Phys. Rev. D.*, 66, 041301
- Mellier Y., 1999, *ARA&A*, 37, 127
- Pen U., Lee J., Seljak U., 2000, *ApJ*, 543, L107
- Pen U., Van Waerbeke L., Mellier Y., 2002, *ApJ*, 567, 31
- Percival W. J. et al., 2002, *MNRAS*, 337, 1068
- Pierpaoli E., Borgani S., Scott D., White M., 2002, *MNRAS*, submitted (astro-ph 0210567)
- Pryke C., Halverson W., Leitch E. M., Kovac J., Carlstrom J. E., Holzapfel W. L., Dragovan M., 2002, *ApJ*, 568, 46
- Reiprich, T. H., Böhringer H., 2002, *ApJ*, 567, 716
- Refregier A., Bacon D. J., 2003, *MNRAS*, 338 48
- Refregier A., Rhodes J., Groth E. J., 2002, *ApJ*, 572, L131
- Schneider P. Van Waerbeke L., Kilbinger M., Mellier Y., 2002, *A&A*, 396, 1
- Schuecker P. Böhringer H., Collins C. A., Guzzo L., 2003, *A&A*, 398, 867
- Seljak U., 2002, *MNRAS*, 337, 769
- Smith R. E., Peacock J. A., Jenkins A., White S. D. M., Frenk C. S., Pearce F. R., Thomas P. A., Efstathiou G., Couchman H. M. P., 2002, *MNRAS*, submitted (astro-ph 0207664)
- Spergel D. N. et al., 2003, *ApJ*, submitted (astro-ph/0302209)
- Stebbins A., 1997, preprint (astro-ph 9609149)
- Taylor A. N., 2001, *Phys. Rev. Lett*, submitted (astro-ph 0111605)
- Taylor A. N., Dye S., Broadhurst T. J., Benitez N., van Kampen E., 1998, *ApJ*, 501, 539
- Tegmark M., de-Oliviera Costa A., 2002, *Phys. Rev. D*, 64, 63001
- Tegmark M., Taylor A. N., Heavens A. F., 1997, *ApJ*, 480, 22
- Van Waerbeke L., Mellier Y., Pelló R., Pen U., McCracken H. J., Jain B., 2002, *A&A*, 393, 369
- Van Waerbeke L., et al., 2001, *A&A*, 374, 757
- Viana P. T., Nichol R. C., Liddle A. R., 2002, *ApJ*, 569, L75
- Wang X., Tegmark M., Zaldarriaga M., 2002, *Phys. Rev. D.*, 65, 123001
- Wolf C., Dye S., Kleinheinrich M., Rix H.-W., Meisenheimer K., Wisotzki L., 2001, *A&A*, 377, 442
- Wolf C., Meisenheimer K., Rix H.-W., Borch A., Dye S., Kleinheinrich M., 2003, *A&A*, 401, 73